

1 **Mesotrode: chronic simultaneous mesoscale cortical imaging and**
2 **subcortical or peripheral nerve spiking activity recording in mice.**

3 Dongsheng Xiao^{1,2}, Yuhao Yan^{1,2}, Timothy H Murphy^{1,2*}

4
5 ¹University of British Columbia, Department of Psychiatry, Kinsmen Laboratory of Neurological
6 Research, Detwiller Pavilion, 2255 Wesbrook Mall, Vancouver, BC V6T 1Z3, Canada

7 ²Djavad Mowafaghian Centre for Brain Health, University of British Columbia, 2215 Wesbrook
8 Mall, Vancouver, BC V6T 1Z3, Canada

9
10 *Correspondence to: Timothy H Murphy

11 Address: 2255 Wesbrook Mall, Detwiller Pavilion, Vancouver, B.C. V6T 1Z3, Canada

12 E-mail: thmurphy@mail.ubc.ca

13
14
15 **Abbreviated title:** Chronic multiscale, multimodal brain/peripheral nerve activity recording in
16 mice.

17
18 **Number of pages:** 31

19 **Number of figures:** 7 (7 Figure Supplements, 5 Video)

20 **Number of words**

21 - **Abstract:** 230

22 - **Introduction:** 654

23 - **Results:** 1847

24 - **Discussion:** 1163

25 - **Methods:** 1837

26

27

28 **Abstract**

29 Brain function originates from hierarchical spatial-temporal neural dynamics distributed across
30 cortical and subcortical networks. However, techniques available to assess large-scale brain
31 network activity with single-neuron resolution in behaving animals remain limited. Here we
32 present Mesotrode that integrates chronic wide-field mesoscale cortical imaging and compact
33 multi-site cortical/subcortical cellular electrophysiology in head-fixed mice that undergo self-
34 initiated running or orofacial movements. Specifically, we harnessed the flexibility of chronic
35 multi-site tetrode recordings to monitor single-neuron activity in multiple subcortical structures
36 while simultaneously imaging the mesoscale activity of the entire dorsal cortex. A mesoscale
37 spike-triggered averaging procedure allowed the identification of cortical activity motifs
38 preferentially associated with single-neuron spiking. Using this approach, we were able to
39 characterize chronic single-neuron-related functional connectivity maps for up to 60 days post-
40 implantation. Neurons recorded from distinct subcortical structures display diverse but
41 segregated cortical maps, suggesting that neurons of different origins participate in distinct
42 cortico-subcortical pathways. We extended the capability of Mesotrode by implanting the micro-
43 electrode at the facial motor nerve and found that facial nerve spiking is functionally associated
44 with the PTA, RSP, and M2 network, and optogenetic inhibition of the PTA area significantly
45 reduced the facial movement of the mice. These findings demonstrate that Mesotrode can be
46 used to sample different combinations of cortico-subcortical networks over prolonged periods,
47 generating multimodal and multi-scale network activity from a single implant, offering new
48 insights into the neural mechanisms underlying specific behaviors.

49

50 **Introduction**

51 System-level mechanisms of cognition and action across networks of single neurons in awake,
52 behaving mice remain largely elusive (Buzsaki, 2006; Aru, Suzuki and Larkum, 2020; Roth and
53 Ding, 2020). The difficulty comes from recording neural activity over large spatial scales but
54 with single neuron resolution during sensory and motor processes (Alivisatos *et al.*, 2012). In the
55 mammalian brain, large-scale cortical network activity is dynamically sculpted by local or long-
56 range inputs from individual neurons in various cortical or subcortical structures (Koch *et al.*,
57 2016). Decoding the principles of neuronal network activity is essential for understanding brain
58 function (Oh *et al.*, 2014; Jiang *et al.*, 2015). One important aspect of such understanding is
59 mapping the functional connectivity of single neurons in relation to cortical networks. Emerging
60 studies using *in vivo* electrophysiological and imaging techniques have revealed that activities of
61 single neurons are functionally coupled to those of local microcircuits or the global cortical
62 networks, and such connectivity is dynamically regulated depending on the behavioral state of
63 the animal (Barson *et al.*, no date; J. L. Chen *et al.*, 2013; Xiao *et al.*, 2017; Clancy, Orsolic and
64 Mrsic-Flogel, 2019). While most of the current studies only provide a snapshot of the
65 connectivity map of a single neuron, the development of procedures where both single-unit
66 activity and large-scale cortical network dynamics of awake-behaving mice can be chronically
67 recorded is desirable.

68

69 Previously, chronic extracellular recordings in rodent brains were achieved most widely using
70 bundled microwires called tetrodes, and more recently extended to the use of high-throughput
71 recording devices such as silicon probes including Neuropixels (Bragin *et al.*, 2000; Nguyen *et al.*,
72 *et al.*, 2009; Vandecasteele *et al.*, 2012; Voigts *et al.*, 2013; Delcasso *et al.*, 2018; Juavinett,

73 Bekheet and Churchland, 2019; Steinmetz *et al.*, 2021). In the case of conventional chronic
74 tetrode recording setups, a common feature is the inclusion of a microdrive that provides axial
75 control over the positioning of the electrodes which allows the electrode position to be adjusted
76 for better recording qualities throughout the experimental periods. However, this microdrive
77 hinders simultaneous wide-field optical imaging of the cortex, making it difficult to investigate
78 the correlation between subcortical single-unit activation and cortical network activity. On the
79 other hand, chronic silicon probe recordings rely on a skull-mounted probe and a large
80 headstage, also have the same limitation of not allowing for simultaneous wide-field imaging.

81

82 To overcome these challenges, we designed the Mesotrode system where we combine *in vivo*
83 electrophysiology via multi-site tetrode implants and mesoscale brain imaging to characterize the
84 functional connectivity of individual cortical or subcortical neurons chronically. We show that
85 these tetrode preparations can obtain high-fidelity, single-unit activity in any cortical or
86 subcortical structure. More importantly, this setup preserves optical access to the entire cranial
87 window of the animal which permits simultaneous functional brain imaging as well as
88 optogenetic manipulation of neuronal activity across the whole dorsal cortex. To obtain high-
89 resolution wide-field imaging of mouse brain activity, we chose to utilize GCaMP6, a genetically
90 encoded Ca^{2+} indicator (GECI) widely used to optically record suprathreshold neuronal
91 activation due to its high sensitivity and optimal signal-to-noise ratio (T.-W. Chen *et al.*, 2013).
92 Furthermore, it has been shown that GECIs can stably report neuronal activity over several
93 months (Huber *et al.*, 2012; Margolis *et al.*, 2012; Silasi *et al.*, 2016), making them ideal for
94 chronic studies of cortical network dynamics. We found that neurons from various subcortical
95 structures, including the hippocampus, thalamus, striatum, and other midbrain areas, display

96 distinct functional connectivity patterns with the cortex. More importantly, we show that the
97 spike-triggered maps (STMs) of recorded neurons can be stable for up to two months. Moreover,
98 we extended Mesotrode to record facial nerve spiking activity and identified a novel cortical
99 network that is causally involved in controlling facial movement, further highlighting the wide
100 applicability of this technique. These results indicate that our Mesotrode can be widely exploited
101 to investigate multiscale functional connectivity within the central nervous system of mice over
102 an extended timescale.

103

104 **Results**

105 **Chronic single-unit recording with wide-field transcranial imaging window.**

106 We developed the Mesotrode implantation procedure with the aim to make them low profile,
107 flexible in location, minimally invasive, and yet stable while maintaining optical access to the
108 entire dorsal cortex such that we can record chronic single neuron activity and mesoscale cortical
109 dynamics simultaneously. Briefly, we fabricated tetrodes from tungsten wires which were then
110 soldered to a miniature connector that was cemented onto the back of the mouse skull during
111 surgery (see Methods). The single tetrode was stiff enough to be straightly inserted into the deep
112 brain areas through a small burr hole (<1mm) (**Figure 1A**). The body of the tetrode that
113 remained outside of the brain was bent parallel to the skull and the minimal size helped preserve
114 optical transparency during imaging sessions (**Figure 1B**). As the miniature connectors are low-
115 profile, mice were group-housed after the surgery (**Figure 1C**), and we did not observe
116 significant damage to the window or the connectors after long-term monitoring. The tetrodes can
117 be flexibly implanted in almost any brain structure of interest, either cortical or subcortical. We
118 have successfully obtained high-quality recordings in the mouse cortex, hippocampus, thalamus,

119 striatum, and midbrain. The recording site of each tetrode is confirmed using *post-hoc*
120 histological analysis (**Figure 1D**). We found that the single unit activity was relatively stable
121 during one week, two weeks, and two months of recordings after implantation (**Figure 1F, G**),
122 which is consistent with previously reported chronic tetrode recordings in mice (Tolias *et al.*,
123 2007; Hong and Lieber, 2019; Kim, Br nner and Carl n, 2020; Voigts *et al.*, 2020).

124
125 We implanted a total of 29 tetrodes in the midbrain, hippocampus, thalamus, striatum, and cortex
126 of 14 mice, and recorded the activity of 110 neurons with simultaneous mesoscale cortical
127 imaging for up to 2 months after implantation (**Figure 2**). We registered all the putative positions
128 of the recorded neurons as well as the tetrode tracks to a 3D mouse brain model, which was
129 reconstructed from an MRI scan (Egan *et al.*, 2015) (**Figure 2A, B**). First, we compared the
130 firing profiles of the neurons from different brain regions. On average, we obtained 3-5 neurons
131 per tetrode implanted, and this yield was consistent across regions (**Figure 2C**). The inter-spike
132 interval (ISI) of neurons recorded from most brain regions ranged between 0.2-0.7s, except for
133 neurons of the striatum, which fires significantly less compared to neurons in other brain regions
134 (**Figure 2D**, $p < 0.05$). The coefficient of variation (CV) of ISI, a metric that indicates the
135 consistency of the firing rate, was similar across brain regions (**Figure 2E**).

136
137 **Spike-triggered average mapping of the thalamus, striatum, hippocampus, and midbrain**
138 **neuron-defined mesoscale cortical networks.**

139 Spike-triggered average mapping (STM) has been previously used to investigate functional
140 connectivity between single spiking neurons and cortical networks (Barson *et al.*, no date; Xiao
141 *et al.*, 2017; Clancy, Orsolich and Mrsic-Flogel, 2019; Liu *et al.*, 2021). However, this has only

142 been achieved using acute preparation. To assess the functional connectivity of the chronically
143 recorded neurons, we combined electrophysiological recordings with simultaneous mesoscale
144 cortical imaging through a bilateral window that encompassed the entire dorsal cortex in head-
145 fixed, awake mice (**Figure 3A, B, Video 1, 2**). To obtain STMs of the recorded neuron, we
146 calculated the peak response of normalized Ca^{2+} activity ($\Delta F/F$) of each pixel averaged between
147 3s before and after ($\pm 3s$) the onset of each spike, which gave us a wide-field mapping of the
148 cortical areas that were associated with spiking activity of the recorded neuron (Xiao *et al.*,
149 2017). Green reflectance signals, which were recorded with the same frequency as the GCaMP6
150 signal, were used to correct hemodynamic artifacts (**Figure 3C, D**).

151
152 We found that single neuron defined functional maps were stable across recording sessions and
153 days. For example, the STM of a hippocampus neuron was associated with the RSP, BCS, and
154 M2 region for 10 recording sessions on different days (**Figure 4A, B**). To better visualize the
155 stability of STMs across recording, we used Mesonet, a machine-learning based toolbox for
156 parcellating brain regions, to accurately align our mesoscale images to a common brain
157 atlas (Xiao *et al.*, 2021). We show that the STMs of a midbrain neuron were relatively stable over
158 2 months (**Figure 4C, D**). The spiking activity of the neuron on different days was highly
159 correlated with the lower limb, upper limb, and trunk sensorimotor areas on both hemispheres of
160 the cortex. To examine the neural correlates of different behaviors, we also incorporated a
161 Raspberry pi camera to monitor the spontaneous behavior of the mice during brain activity
162 recordings (**Figure 4C, E**). In this example, we show that the instantaneous firing rate and
163 patterns of this midbrain neuron were highly correlated with the paw movement of the mouse,
164 consistent with our finding that this neuron is functionally associated with the limb sensorimotor

165 areas. These results highlight the power of this multimodal approach, in that it can link high-
166 resolution single neuron activity with network dynamics of the entire cortex and concurrent
167 animal behavior, which greatly improves our ability to dissect the functional role of individual
168 neurons of any brain region.

169

170 To quantify the distribution of distinctively patterned STMs of neurons across brain regions, we
171 applied a graph-based clustering algorithm, Phenograph, on z-scored STMs (Levine *et al.*, 2015)
172 (**Figure 5**). In total, we included 1146 STMs of 110 neurons recorded during multiple sessions.
173 This resulted in 10 clusters with each cluster representing a distinct STM pattern evidenced by
174 their within-cluster averaged map (**Figure 5A**). Un-matched STMs that were below the
175 similarity threshold (Pearson's correlation < 0.3) compared to any of the 10 cluster average maps
176 were excluded (94 out of 1146 STMs). For all clusters, individual STMs within the clusters
177 showed high similarity to the cluster average maps (**Figure 5B**). In order to validate the optimal
178 number of clusters for partitioning our dataset, we evaluated the clustering effectiveness of a
179 varied number of clusters when applying K-means clustering algorithm using Silhouette score
180 (Rousseeuw, 1987) and confirmed that 10 clusters are most appropriate (**Figure 5C**). Degrees of
181 separation between clusters were visually inspected by projecting dimensionally reduced STMs
182 onto 3D space using t-distributed stochastic neighbor embedding (t-SNE), a commonly used
183 statistical method for plotting high-dimensional data points onto 3D space (**Figure 5D**).

184

185 **Figure 5E** shows the proportions of STMs of neurons in different brain regions that were
186 assigned to each cluster. We found that STMs in each region exhibited a stereotypical
187 distribution pattern. For example, STMs of cortical neurons were primarily assigned to clusters

188 #1-3 and #5-7, corresponding to motor, barrel, and primary somatosensory cortex activation
189 patterns. These activation areas also matched the locations of the recorded cortical neurons (e.g.
190 motor cortical neurons showed motor area activated STMs), suggesting that the functional
191 connectivity patterns of cortical neurons were localized to cortical areas surrounding the
192 recorded neuron, which is consistent with previous reports (Xiao *et al.*, 2017; Clancy, Orsolio
193 and Mrcic-Flogel, 2019). Hippocampal neurons primarily displayed STMs with retrosplenial
194 cortex activation (cluster#10, 59.6% of all hippocampal neuron STMs), reaffirming the dense
195 functional connectivity between these two regions (Karimi Abadchi *et al.*, 2020). STMs of
196 striatal neurons were dominated by two opposing patterns, where 47.7% of them showed a global
197 activation except for the body (limb and trunk) somatosensory regions (cluster#4) and 28.8% of
198 them showed only activation in the body sensory regions (cluster#9). Thalamic neurons
199 exhibited diverse STM patterns with the primary activated regions in lateral anterior cortical
200 regions (cluster#5, 5.6%, cluster#6, 23.3%, cluster#7 26.3% of all thalamic STMs) and medial
201 cortical regions (cluster#8, 6.5%, cluster#9, 11.6%, cluster#10, 9.9% of all thalamic STMs). This
202 suggested that thalamic neurons had diverse functional connectivity patterns in relation to the
203 dorsal cortex, consistent with previous studies (Xiao *et al.*, 2017). STMs of midbrain neurons
204 were most assigned to cluster#8 with medial frontal and somatosensory cortex activation
205 (cluster#8, 44.6% of all midbrain STMs), but also included functional connectivity patterns with
206 various other cortical regions (cluster#6, 10.5%, cluster#9, 12.6%, cluster#10, 11.2% of all
207 midbrain STMs). Interestingly, we found that neurons of different subcortical origins sometimes
208 have overlapping STMs (e.g. cluster#9, and #10 exhibited by neurons from all subcortical
209 regions), which suggests that they may be involved in the same subcortico-cortical functional
210 pathway (**Figure 5E**). Taken together, these findings highlighted the capability of Mesotrode to

211 capture the diverse cortical functional connectivity patterns of neurons across brain regions using
212 chronic electrodes.

213

214 **Linkage of spiking peripheral nerve to specific mesoscopic cortical maps**

215 One key advantage of using our minimally invasive micro-electrode setup is the flexibility of the
216 location where they can be implanted and the relatively small footprint at the insertion site. This
217 allows us to explore the functional connectivity of neurons that are otherwise difficult to study.
218 For example, it's difficult to simultaneously record the neural activity of the facial motor nucleus
219 and cortex in order to investigate the cortico-brainstem motor pathways that directly innervate
220 facial muscles that control whisker movement and facial expressions in mice (Petersen, 2014;
221 Sreenivasan *et al.*, 2016; Mercer Lindsay *et al.*, 2019). Here, we implanted micro-wires on the
222 facial motor nerve to record the spiking activity of the axonal projections from the facial motor
223 neurons (**Figure 6A, B**). We obtained the STMs of facial motor nerves by simultaneous wide-
224 field imaging of GCaMP6 mice (n = 5 mice). Surprisingly, we found a distinct cortical pattern,
225 activation in RSP, M2, and PTA areas (**Table 1**), associated with facial motor nerve spiking
226 activity (**Figure 6C, D, and E, Figure 6—figure supplement 1, Video 3**) in awake mice
227 showing spontaneous movements. Using automated light-based mapping technology (Ayling *et*
228 *al.*, 2009), we found a broad area of the dorsal cortex, including the PTA region could evoke
229 facial motor nerve spiking activity when optogenetically stimulated (**Figure 6F, G, and H,**
230 **Figure 6—figure supplement 2-7, Video 4**) within Thy1-ChR2 mice (n = 6 mice). To further
231 investigate causal relationships, we directly inhibited the PTA by optogenetically stimulating
232 inhibitory neurons of the PTA region of VGAT-ChR2 mice (n = 3 mice). Echoing our previous
233 finding, inhibiting the PTA not only stopped the PTA neurons from firing but also prevented the

234 facial movements of these mice when the blue light stimulation was on (**Figure 7, Video 5**). To
235 eliminate the possibility that this observation is due to indirect inhibition of other brain areas, we
236 simultaneously recorded neuronal activities in M1 and the barrel cortex (BCS). We confirmed
237 that the neuron firing in these brain areas was not decreased by PTA inhibition (**Figure 7A, B**).
238 More interestingly, we saw a “rebound effect”, a sudden increase in PTA neuron firing and facial
239 movement, right after the stimulation is turned off (**Figure 7C, D**). This “off response” supports
240 the causal relationships between PTA and facial movement. These findings are consistent with
241 the previous report that the PTA is involved in controlling active movements (Chapman *et al.*,
242 2002; Cohen and Andersen, 2002; Rathelot, Dum and Strick, 2017; Auffret *et al.*, 2018; Lyamzin
243 and Benucci, 2019; Lee *et al.*, 2022). It also underscores that our chronic tetrode implants in
244 combination with optogenetics and optical imaging can be a powerful tool in mapping and
245 identifying novel functional pathways.

246

247 **Discussion**

248 How activities of individual neurons contribute to brain-wide population dynamics remains
249 poorly understood (Brecht *et al.*, 2004; Rancz *et al.*, 2007; Houweling and Brecht, 2008; Packer
250 *et al.*, 2015). It is additionally challenging to study long-range connectivities (e.g. those between
251 subcortical and cortical structures) given the extraordinary complexity of neuronal wiring
252 between brain regions. Non-invasive methods such as fMRI have generated important
253 connectivity models, such as the default mode network (DMN) model, which advanced our
254 understanding of how distinct brain regions communicate with each other during different
255 behavioral contexts (White *et al.*, 2011; Gutierrez-Barragan *et al.*, 2022). However, these
256 methods typically lack the spatial and temporal resolution to understand the connectivity patterns

257 of individual neurons. On the other hand, for more invasive techniques such as viral tracing,
258 although they often provide detailed characterizations of the anatomical patterns between brain
259 areas, the nature of the preparation for these techniques precludes gaining insights into the
260 dynamic nature of the connectivity rules. In this study, we developed the Mesotrode that
261 combined chronic tetrode recording with mesoscale Ca^{2+} imaging to characterize mesoscale
262 connectivity patterns of individual neurons. We showed that the functional connectivity patterns
263 of individual neurons are relatively stable in the same behavioral state, and neurons from
264 different brain regions display distinct distributions of these patterns. We further showcased the
265 utility of our procedure by recording from the facial motor nerve and found a distinct cortical
266 activation associated with facial nerve activity. Additionally, Mesotrode provides a wide-field
267 access window for optogenetic stimulations. We showed a causal link between PTA activity and
268 facial movement in mice. These findings established that our multimodal recordings combining
269 chronic electrophysiology, mesoscale imaging, optogenetics, and behavioral characterization can
270 be widely applied to further our understanding of neuronal connectivity and behaviors.

271

272 **Compared to other chronic recording setups**

273 Our approach adds to the plethora of techniques previously described to characterize long-range
274 functional connectivity by combining single-neuron activity recording and mesoscale cortical
275 imaging. These techniques typically differ in how and where the individual neurons' activities
276 are recorded. For instance, Barson et.al used two-photon imaging to record individual cortical
277 neurons' activities, which allows differentiation of different neuronal types through genetic
278 manipulation (Barson *et al.*, no date), but it has lower temporal resolution and is restricted to
279 recording cortical neurons. Xiao et.al, Clancy et.al, Peters et.al, and Liu et.al all used either

280 silicon probes or neuropixel probes to record large populations of cortical or subcortical neurons
281 (Xiao *et al.*, 2017; Clancy, Orsolich and Mrsic-Flogel, 2019; Liu *et al.*, 2021; Peters *et al.*, 2021),
282 but it remains difficult to use these setups to track activities of the same neurons over days. In
283 addition to these approaches, we can use our chronic tetrode implantation to track neuronal
284 activities at multiple brain regions over long periods of time to better describe the dynamic
285 nature of global neuronal affiliations; however, the number of neurons that can be recorded per
286 tetrode is limited which does reduce our data acquisition throughput.

287
288 Compared to most of the previously reported chronic tetrodes setups with the inclusion of a
289 microdrive, our approach has the unique advantages that setting up the apparatus and implanting
290 the tetrodes is a lot more straightforward, mini-connector enables group housing and it is
291 compatible with overhead cameras which permits simultaneous optical interrogation of neuronal
292 circuits (Battaglia *et al.*, 2009; Nguyen *et al.*, 2009; Voigts *et al.*, 2013; Billard *et al.*, 2018;
293 Delcasso *et al.*, 2018; Voigts and Harnett, 2020). However, it does come with the price that the
294 tetrode cannot be moved after it is implanted, which means that the implant would fail if the
295 health of the neuron deteriorates too much over time. Albeit, since our goal is to record the
296 activity of the same neurons, we deemed it a worthy tradeoff for our purpose.

297
298 **Variability of spike-triggered average maps in different brain regions**
299 Activities of cortical pyramidal neurons are known to be coupled to local network activity; as
300 such, STMs of these neurons often display activity motifs localized to the cortical regions they
301 reside, indicating that their functional connections are mostly involved in local networks (Xiao *et al.*
302 *et al.*, 2017; Clancy, Orsolich and Mrsic-Flogel, 2019). On the other hand, subcortical neurons (i.e.

303 thalamic neurons) can display more diverse and distal connectivity patterns with cortical
304 networks that are less confined by their locations (Xiao *et al.*, 2017). Here, we extended these
305 characterizations to more subcortical regions (i.e. striatum, hippocampus, and midbrain), and
306 found that these neurons, similar to thalamic neurons, generate functionally diverse STMs. This
307 can be attributed to the diverse cell types within these structures (Phillips and Irvine, 1979;
308 Cembrowski *et al.*, 2016). Furthermore, by classifying these STMs, we found that the
309 connectivity patterns of neurons in different subcortical structures are varied. For instance, STMs
310 of midbrain neurons can be primarily categorized into 4 classes, with each class having distinct
311 activity motifs, which is in contrast to the striatum neurons, the STMs of which are grouped into
312 only two main classes. More interestingly, STMs of different subcortical regions display low
313 levels of overlap, suggesting that neurons of different subcortical origins form their own distinct
314 connectivity pattern to the cortex.

315

316 **The spike-triggered average map associated with specific brain function**

317 The single neuron defined functional maps (STMs) can reveal functional cortical architecture
318 related to the activity of individual cortical and subcortical-cortical neurons (Xiao *et al.*, 2017).
319 The distinct STM patterns indicate that single neuron embedded large-scale subcortico-cortical
320 networks may be associated with specific brain functions (Pessoa, 2014; Liu, Leopold and Yang,
321 2021; Amunts *et al.*, 2022). To explore this possibility, for the first time, we simultaneously
322 record the output spiking activity of the facial motor nucleus and wide-field calcium dynamics of
323 the cortex, which enable us to investigate the cortico-brainstem motor pathways that directly
324 control facial movements in mice. Interestingly, we found that facial nerve spike-triggered
325 average map functionally associated with active facial movements, and the causal relationship

326 can be tested by optogenetic stimulation or inhibition of the PTA area. Previous studies using
327 anterograde virus tracing have revealed that the motor cortex sends few direct projections to the
328 facial nucleus while the most prominent projections from the motor, somatosensory, and
329 association cortex are polysynaptic, presumably through nuclei in the brainstem (Grinevich,
330 Brecht and Osten, 2005; Matyas *et al.*, 2010; Rathelot, Dum and Strick, 2017). Studies in
331 humans and monkeys have identified parietal-eye-field and reach-specific areas that involve
332 voluntary control of eye or hand movement (Lynch, 1980; Andersen, 1989; Sakata *et al.*, 1997;
333 Chapman *et al.*, 2002; Konen and Kastner, 2008; Archambault, Caminiti and Battaglia-Mayer,
334 2009; Pouget, 2015; Rathelot, Dum and Strick, 2017). Our findings suggest that the PTA region
335 is also involved in facial movements in mice, and supplement the current understanding of the
336 functional connectivity between cortex and facial nucleus motor neurons.

337

338 **Conclusion**

339 Our results demonstrated that our minimally invasive, flexible, low profile, low cost, chronically
340 implanted Mesotrode can be readily applied to interrogating the functional connectivity between
341 single neurons and large-scale cortical networks, and the causal relationship can be tested by
342 optogenetic stimulation.

343

344 **Materials and methods**

345 **Mice**

346 Animal protocols (A13-0336 and A14-0266) were approved by the University of British
347 Columbia Animal Care Committee and conformed to the Canadian Council on Animal Care and
348 Use guidelines and animals were housed in a vivarium on a 12 h daylight cycle (7 AM lights on).

349 Most experiments were performed toward the end of the mouse light cycle. Transgenic
350 GCaMP6s mice (males, 2–4 months of age, weighing 20–30g; n=19) were produced by crossing
351 *Emx1-cre* (B6.129S2-*Emx1*^{tm1(cre)Kry}/J, Jax #005628), *CaMK2-tTA* (B6.Cg-Tg(Camk2a-
352 tTA)1Mmay/DboJ, Jax #007004) and TITL-GCaMP6s (Ai94;B6.Cg-*Igs7*^{tm94.1(tetO-GCaMP6s)Hze}/J,
353 Jax #024104) strain. The presence of GCaMP expression was determined by genotyping each
354 animal before each surgical procedure with PCR amplification. These crossings are expected to
355 produce a stable expression of the calcium indicator (T.-W. Chen *et al.*, 2013) specifically within
356 all excitatory neurons across all layers of the cortex (Vanni and Murphy, 2014).
357 Channelrhodopsin-2 transgenic mice (Arenkiel *et al.*, 2007) (n = 6) were obtained from the
358 Jackson Labs (line 18, stock 007612, strain B6.Cg-Tg(Thy1-COP4/EYFP)18Gfng/J). Neuronal
359 activity was driven by optically activating inhibitory neurons targeted in VGAT-ChR2-YFP
360 expressing mice (Zhao *et al.*, 2011) (n = 3). No method of randomization was used since all mice
361 belonged to the same sample group. Samples sizes were chosen based on previous studies using
362 similar approaches (Mohajerani *et al.*, 2013; Vanni and Murphy, 2014). Given the use of
363 automated acquisition and analysis procedures, we did not employ blinding.

364

365 **Tetrode fabrication**

366 Polyimide insulated, tungsten wire (40 cm long, diameter 25 μ m, Stablohm 650, California Fine
367 Wire, USA) was folded into four wires and clamped together with the modified alligator clip.
368 The loop of wires was hung over the horizontal bar. The alligator clip was placed into the
369 motorized stage. Eighty clockwise twists were applied and followed by forty counter clock-wise
370 twists to the wire bundle over the course of approximately three minutes. After tetrode twisting
371 was completed, the wires were fused together by heating from three different angles with a heat

372 gun (420°C or 790°F), using medium-low flow. For each angle, begin 1-2 cm below where the
373 wire bundle splits, the heat gun was held 2 cm away from the wire and moved periodically over
374 the length of the wire for about 5 s. The tetrode was removed from the twisting apparatus by
375 gently lifting the alligator clip to relieve tension on the tetrode, and cutting the tetrode near the
376 alligator clip. At the other end, the loop was cut off such that there were four non-bonded strands
377 of wire of equal length. The tetrode was then soldered to a miniature connector using a fine-tip
378 soldering iron (Thermaltronics M8MF375 Micro Fine 0.25 mm).

379

380 **Surgical procedures**

381 Mice were anesthetized with isoflurane (4% for induction and 1.5% for maintenance in air). The
382 eyes were covered with eye lubricant (Lacrilube; www.well.ca) and body temperature was
383 maintained at 37 °C with a heating pad with feedback regulation. Mice were then placed in a
384 stereotaxic frame and received an injection of Lidocaine (0.1ml, 0.2%) under the scalp. Mice
385 also received a 0.5 ml subcutaneous injection of a saline solution containing buprenorphine (2
386 mg/ml), atropine (3µg/ml), and glucose (20 mM). Respiration rate and response to toe pinch
387 were checked every 10-15 min to maintain the surgical anesthetic plane. A skin flap extending
388 over both hemispheres approximately 8 mm in diameter (3 mm anterior to bregma to the
389 posterior end of the skull and down lateral to eye level) was cut and removed. Fascia or
390 connective tissue is lightly scraped away from the skull and small (< 1 mm diameter) holes are
391 drilled through the skull, using a high-speed dental drill with a sterile bit, over the cortex.
392 Tetrode was directed toward the center of the hole and placed in the target using a motorized
393 micromanipulator (MP-225, Sutter Instrument Company). Miniature connectors (2 x 2 x 2 mm)
394 are cemented to the skull (with dental adhesive) around the imaging window (the total weight is

395 < 1 gm). Ground and reference electrodes are fixed into place on the surface of the posterior
396 skull.

397

398 After tetrode implantation, the chronic transcranial window was implanted as previously
399 described (Silasi *et al.*, 2016). Briefly, the skin between the ears and the eyes was properly
400 cleaned with Betadine dissolved in water and ethanol. The skin covering the occipital, parietal
401 and frontal bones was cut away. The fascia and any connective tissue on the skull surface were
402 gently wiped off. C&B-Metabond transparent dental cement (Parkell, Edgewood NY, USA;
403 Product: C&B Metabond) was prepared in a ceramic bowl and used to glue a head-fixing
404 titanium bar to the cerebellar plate or a 4/40 stainless steel setscrew slightly angled posteriorly
405 (~120° relative to skull). With the bar or the setscrew in place, a thick layer of dental adhesive
406 was applied to the skull. A coverglass (Marien-feld, Lauda-Konigshofen, Germany; Cat n:
407 0111520) previously cut to the size of the final cranial window (~8 mm diameter), was placed on
408 top of the dental cement before it solidified, preventing the formation of bubbles. The cement
409 remains transparent after it solidifies and the surface vasculature should be readily seen through
410 the final result.

411

412 **Recovery and post-operative monitoring**

413 At the end of the surgical procedures, mice received a subcutaneous injection of saline (0.5 ml)
414 with 20 mM of glucose and were allowed to recover in their home cages with an overhead heat
415 lamp. The activity level of mice that underwent the procedure was monitored hourly for the first
416 4 h and every 4-8 h thereafter. Mice are allowed to recover for 7 days from the window
417 implantation before performing electrophysiology recording.

418

419 **Electrophysiology data acquisition**

420 For Electrophysiology recordings, a custom adapter was connected to the miniature connector.

421 The tetrode signals were amplified using a 16-channel data acquisition system (20 kHz, USB-

422 ME16-FAI-System, Multi-Channel Systems) and recorded for at least 30 min every day.

423

424 Raw extracellular traces were imported into Spike2 (Cambridge Electronic Design, Cambridge,

425 UK) or SpikeSorter software (Swindale and Spacek, 2014; Swindale *et al.*, 2021) for spike

426 sorting and analysis. Briefly, data were high pass-filtered at 1kHz, and excitatory spikes were

427 detected using a threshold of 4.5 times the median of the standard deviation over 0.675. Sorting

428 was carried out by an automated method previously described (Swindale and Spacek, 2014) and

429 followed by manual visual inspection of units.

430

431 **Wide-field calcium imaging**

432 All mice were habituated for 1 week prior to data collection. Awake mice were head-fixed and

433 placed on a wheel in a dark imaging chamber for data collection. A behavioral camera

434 (Raspberry Pi camera) and an infrared light were placed inside the imaging chamber to monitor

435 active behaviors, such as running or whisking. A Pantera 1M60 CCD camera (Dalsa) was

436 equipped with two front-to-front lenses (50 mm, f $\frac{1}{4}$ 1.4:35 mm, f $\frac{1}{4}$ 2; Nikon Nikkor) and a

437 bandpass emission filter (525/36 nm, Chroma). The 12-bit images were captured at a frame rate

438 of 120 Hz (exposure time of 7 ms) with 8×8 on-chip spatial binning using EPIX XCAP v3.8

439 imaging software. The cortex was sequentially illuminated with alternating blue and green LEDs

440 (Thorlabs). Blue light (473 nm) with a bandpass filter (467 to 499 nm) was used to excite

441 calcium indicators and green light (525 nm) with a bandpass filter (525/50 nm) was used to
442 observe changes in cerebral blood volume. The blue and green LEDs were sequentially activated
443 and synchronized to the start of each frame's exposure period with transistor-transistor logic
444 such that each frame collected only fluorescence or reflectance signals at 60 Hz each. This LED
445 strobe frequency of 60 Hz exceeded the critical flicker fusion frequency for mice, which marks
446 the highest temporal frequency that an observer can resolve flicker before it becomes
447 indistinguishable from constant light and was likely imperceptible to the mice. Reflectance
448 signals were subtracted from fluorescence signals to mitigate the contribution of hemodynamics
449 to fluorescence signals.

450

451 **Optogenetic stimulation protocols**

452 Inhibitory neurons in the cortex were optogenetically manipulated separately in VGAT-ChR2
453 mice. A 473nm laser (Crystal Laser BCL-473-050, Reno, NV, USA) was connected to a fiber
454 optic patch cable (0.22 NA, 200 μ m gauge; Thorlabs FG200UCC, USA). During the experiment,
455 1 mW (measured from the end of the cable) of optical stimulation was delivered for an overall
456 time of 10 s. For automated Thy1-ChR2-based facial motor mapping, we chose a relatively
457 collimated 473 nm laser targeted through a simple microscope. The laser was moved in random
458 order to each of the predefined stimulation locations (8x8 grid) and delivered a flash of laser
459 light (10 ms, 2.0 mW) to each point while collecting facial motor nerve response.

460

461 **Spike-triggered average maps (STM) Clustering**

462 We employed an unsupervised clustering algorithm, PhenoGraph (Levine *et al.*, 2015), to
463 categorize STMs. The graph was built in 2 steps: 1) it finds k nearest neighbors for N input

464 vectors (4096 dimensions for 64x64 STMs) using Euclidean distance, resulting in N sets of k
465 nearest neighbors, 2) a weighted graph is built where the edge weight between pairs of nodes
466 depends on the number of neighbors they share. We then perform Louvain community detection
467 (Blondel *et al.*, 2008) on this graph to partition the graph that maximizes modularity. This
468 algorithm only requires one input parameter which is k, the number of nearest neighbors to be
469 found for each input vector, and the resulting number of clusters (10) is relatively insensitive to
470 the k chosen over the range of typically chosen values. We also performed k-means clustering
471 using the same input and compared clustering effectiveness using the Silhouette score and found
472 that 10 clusters were optimal. We then performed a cluster identity refinement step, where an
473 individual STM whose similarity (Pearson correlation value) with the cluster average STM of the
474 assigned cluster was lower than 0.3 was manually reassigned if its similarity with group average
475 STMs of any other clusters was higher than 0.3; otherwise, that STM was excluded. A total of 94
476 out of 1146 STMs (8.2%) were excluded.

477

478 **Histology**

479 At the end of each experiment, animals were killed with an intraperitoneal injection of
480 pentobarbital (24 mg). Mice were transcardially perfused with PBS followed by chilled 4% PFA
481 in PBS. Coronal or sagittal brain sections (50 μ m thickness) were cut on a vibratome (Leica
482 VT1000S). Images of brain tissues with counter-stained DAPI were acquired using confocal
483 microscopy (Zeiss LSM510) to reveal the electrode track and help identify the approximate
484 cortical/subcortical location of recorded cells.

485

486 **Statistical analysis**

487 Statistical analyses were performed using GraphPad Prism, Version 9. Statistical tests and results
488 are reported in the figure legends. More than two groups were compared using one-way ANOVA
489 followed by Dunnett's test comparing experimental flies to each control. All graphs represent
490 mean \pm SEM. Sample sizes are listed in the figure legends. No explicit power analyses were used
491 to determine sample sizes prior to experimentation. Minimum sample sizes were decided prior to
492 experimentation based on previous experience or pilot experiments revealing how many samples
493 are typically sufficient to detect reasonable effect sizes.

494

495 **Data and code availability**

496 All code used for data analysis and sample data generated in this study have been deposited in
497 the Open Science Framework repository (<https://osf.io/67p3s/>).

498

499 **Acknowledgements**

500 This work was supported by a Canadian Institutes of Health Research (CIHR) Foundation Grant
501 FDN-143209 and project grant to T.H.M. and the UBC Institute of Mental Health Marshall
502 Scholars and Fellowship program. THM was also supported by the Brain Canada
503 Neurophotonics Platform, a Heart and Stroke Foundation of Canada grant in aid, National
504 Science and Engineering Council of Canada (NSERC; GPIN-2022-03723), and a Leducq
505 Foundation grant. This work was supported by resources made available through the Dynamic
506 Brain Circuits cluster and the NeuroImaging and NeuroComputation Centre at the UBC Djavad
507 Mowafaghian Centre for Brain Health (RRID SCR_019086) and made use of the DataBinge
508 forum. D.X. was supported by the Michael Smith Foundation for Health Research. We thank

509 Pumin Wang, and Cindy Jiang for surgical assistance, Jamie D Boyd for technical assistance. We
510 thank Hongkui Zeng and Allen Brain Institute for providing transgenic mice.

511

512 **Competing interests**

513 The authors declare no competing interests.

514

515 **Author contributions**

516 Dongsheng Xiao, Conceptualization, Data curation, Software, Formal analysis, Visualization,
517 Methodology, Writing – original draft, Writing – review and editing; Yuhao Yan, Formal
518 analysis, Visualization, Methodology, Writing – original draft, Writing – review and editing;
519 Timothy H Murphy, Conceptualization, Supervision, Funding acquisition, Investigation,
520 Visualization, Methodology, Project administration, Writing – review and editing.

521

522 **Figure legends**

523 **Figure 1. Chronic tetrodes recording compatible with mesoscale transcranial Imaging.** (A)
524 Images of skull surface during tetrode implantation. Panels depict the location of 4 tetrodes
525 placed in skull burr holes using a micromanipulator. (B) Image showing transcranial window
526 with tetrodes placed in the striatum, thalamus, and midbrain. (C) Chronic tetrode recording is
527 compatible with group-housed mice. (D) Post-mortem histology is performed to confirm the
528 tetrode location. (E) Cartoon of tetrode and local neurons. (F) Example of long-term recording
529 using transcranial imaging window plus tetrodes. (G) Sorted spikes from (F) (brown, blue, and
530 gray indicate 1 week, 2 weeks, and 2 months after tetrode implantation).

531

532 **Figure 2. Group statistics on tetrode implantation across mice.** (A) Labels corresponding to
533 mouse IDs (n = 14 mice) were registered to a 3D mouse brain model based on tetrode locations.
534 (B) Side view of the 3D reconstruction of 29 tetrode tracks implanted in 14 mice registered to the
535 3D mouse brain model. (C) The mean number of well-isolated neurons recorded per tetrode
536 implanted in different brain regions. (D) Mean inter-spike interval (ISI) of neurons recorded in
537 different brain regions (Dunn's Multiple Comparison Test, striatum vs midbrain, $P < 0.01$,
538 thalamus vs midbrain, $P < 0.05$, n = 14 mice). (E) Mean coefficient of variation of ISIs of
539 neurons across brain regions (Dunn's Multiple Comparison Test, thalamus vs hippocampus, $P <$
540 0.05, n = 14 mice).

541
542 **Figure 3. Recording setup and example spike-triggered average maps.** (A) Illustration of
543 experiment setup incorporating wide-field imaging, and tetrode recording with simultaneous
544 behavioral monitoring. (B) Example tetrodes implantation in the thalamus, BCS1, and striatum.
545 The middle and bottom panel shows the tetrode location registered in a 3D model of the mouse
546 brain. (C) Spike-triggered average of GCaMP6s fluorescence (left), hemodynamic signal
547 (middle, green reflectance), and hemodynamic-subtracted cortical maps (right) of thalamic,
548 BCS1, and striatal neurons. (D) Average traces of GCaMP6s epi-fluorescence (blue),
549 hemodynamic signal (green reflectance), and hemodynamic-subtracted signal (red) surrounding
550 spikes of single neurons, and random trigger average traces (black).

551
552 **Figure 4. Chronic spike-triggered average maps of hippocampus and midbrain neurons.**
553 (A) Unfiltered brain RGB image showing the position of the tetrode (left), GCaMP6
554 fluorescence image (middle), and histology showing the recording site of the tetrode (right). (B)
555 Example raw and high-pass filtered (> 300 Hz) electrophysiological traces of hippocampal
556 recording 7 days after tetrode implantation and STMs of the hippocampal neuron across
557 recording sessions(top). Another day of hippocampal recording and STMs of the hippocampal
558 neuron across recording sessions(bottom). (C) Unfiltered brain RGB image showing the position
559 of the tetrode (top) and behavior video recording (bottom). (D) Top: Ca^{2+} images recorded 1
560 week (left), 2 weeks (middle), and 2 months (right) after tetrode implanted in the midbrain
561 overlaid with automatically registered brain atlas using Mesonet. Bottom: STMs of the midbrain
562 neuron recorded at the same time points as Top. (E) Synchronized traces of paw movements,
563 instantaneous firing rate, and electrophysiological signals of the midbrain neuron are shown in
564 (C).

565
566 **Figure 5. Clustering STMs of cortical/subcortical neurons.** (A) Average z-scored STM of
567 each cluster. Each cluster represents a unique cortical functional network that individual neurons
568 were associated with. STMs of the same neurons recorded during different sessions were
569 included (1146 total STMs from 110 neurons of 14 mice). (B) Box plot showing the correlation
570 between individual STM and average STM of its assigned cluster. (C) Silhouette coefficient of
571 varying numbers of clusters to validate the optimal number of clusters. (D) 3D-t-SNE plot
572 showing dimensionality reduced representation of clustered individual STMs. (E) The proportion
573 of neurons in each cortical and subcortical region assigned to each STM cluster.

574
575 **Figure 6. Spike-triggered and optogenetics mapping facial nerve spiking associated**
576 **cortical maps.** (A) Mouse anatomy illustrates facial motor nucleus axons (facial nerve) that
577 innervate facial muscles. Micro-wire was implanted in the facial nerve. (B) Example spiking
578 activity recorded from facial motor nerve using the micro-wire. (C) Example calcium imaging
579 during facial nerve recording. (D) Facial nerve spike-triggered average map temporal dynamics
580 surrounding facial nerve spikes ($t = 0$ ms) of a single mouse (top row) or the average of 5 mice
581 (bottom row). (E) Reference atlas (white outlines; ©2004 Allen Institute for Brain Science.
582 Allen Mouse Brain Atlas. Available from: <http://mouse.brain-map.org/>) (F) Illustration of
583 automated light-based mapping of the dorsal cortex (8x8 grid) by photoactivation of Thy1-ChR2
584 mice. (G) Example single trial facial nerve response after light stimulation. (H) Average change
585 of facial nerve responses of 6 mice represented on a 2D color-coded map corresponding to each
586 stimulation coordinate overlaid on an example cortical image of Thy1-ChR2 mouse. The

587 amplitude of the average change for each stimulation coordinate corresponds to the total variance
588 of all the trials (>5 trials, within 200 ms after stimulus) where there is no facial nerve spiking
589 before the stimulus.

590

591 **Figure 7. Optogenetic inhibition of the PTA area significantly reduced the facial movement**
592 **of the mouse.** (A) Unfiltered brain RGB image showing the position of the tetrodes. (B)
593 Simultaneous cellular electrophysiological recording in the cortical regions of M1, BCS, and
594 PTA with optogenetic inhibition on the PTA region. (C) Behavioral image showing masks used
595 for facial movement detection (top). Brain image of a VGAT-ChR2 mouse (ChR2 expressed in
596 cortical inhibitory neurons) with laser targeting the PTA area (bottom). (D) Synchronized traces
597 of optogenetic activation of PTA inhibitory neurons, facial movement, and LFP of the PTA
598 region. Inhibiting the PTA region strongly inhibited facial nerve activity. Cessation of PTA
599 inhibition reliably induced rebound PTA neuron firing and facial movements. (E) The neuronal
600 firing of 12 trials of optogenetic inhibition in PTA. (F) Facial movements ((gradient-
601 mean)/mean) 3s before, 3s during, and 3s immediately after optogenetic inhibition in PTA for 29
602 trials (Dunn's Multiple Comparison Test, $p < 0.001$, $n = 3$ mice).

603

604 **Table 1. Abbreviation used to define different cortical/sub-cortical areas**

Mop (M1)	primary motor area
Mos (M2)	secondary motor area
SSp-m	primary somatosensory area, mouse
SSp-ul	primary somatosensory area, upper limb
SSp-ll	primary somatosensory area, lower limb
SSp-n	primary somatosensory area, nose
SSp-bfd	primary somatosensory area, barrel field
SSp-tr	primary somatosensory area, trunk
VISp	primary visual area
VISa	anterior visual area
VISam	anteromedial visual area
VISpm	posteromedial visual area
VISrl	rostrolateral visual area
VISal	anterolateral visual area
VISI	lateral visual area
RSP	retrosplenial area
AUD	auditory areas
PTA	parietal association area
HPF	hippocampal formation
VTA	ventral tegmental area

605

606 **Video 1.** Video of the 4D spatiotemporal whole-brain dynamics of mesoscale cortical calcium
607 imaging and subcortical neuronal firing. Brain activity data was registered in a 3D mouse brain
608 model. Calcium dynamic intensity and neuronal firing rate of subcortical neurons (Top) were
609 color-coded in the ROIs in the 3D mouse brain model (bottom left). The calcium dynamic was
610 overlaid on a cortical atlas (bottom right).

611
612 **Video 2.** Simultaneous recording of behavior video (left), L-VTA neuronal firing (middle), and
613 wide-field calcium imaging (right) in a behaving mouse.

614
615 **Video 3.** Simultaneous recording of behavior video (left), facial nerve spiking activity (middle),
616 and wide-field calcium imaging (right) during mouse whiskering.

617
618 **Video 4.** Video of the facial response after optogenetic stimulation (blue laser, 10 ms) of PTA in
619 a Thy1-ChR2 mouse.

620
621 **Video 5.** Video of the facial response after optogenetic inhibition (blue laser, 10 s) of PTA in a
622 VGAT-ChR2 mouse.

623

624 **Supplemental Figure legends**

625

626 **Figure 6—figure supplement 1.** Facial nerve spike-triggered average maps of 5 mice.

627
628 **Figure 6—figure supplement 2.** Optogenetic mapping of facial nerve responses (blue laser, 10
629 ms, 2.0 mW) in a Thy1-ChR2 mouse. Averaged responses (> 5 trials) were normalized to the
630 range of 0 and 1 (right).

631
632 **Figure 6—figure supplement 3.** Optogenetic mapping of facial nerve responses (blue laser, 10
633 ms, 2.0 mW) in a Thy1-ChR2 mouse. Averaged responses (> 5 trials) were normalized to the
634 range of 0 and 1 (right).

635
636 **Figure 6—figure supplement 4.** Optogenetic mapping of facial nerve responses (blue laser, 10
637 ms, 2.0 mW) in a Thy1-ChR2 mouse. Averaged responses (> 5 trials) were normalized to the
638 range of 0 and 1 (right).

639
640 **Figure 6—figure supplement 5.** Optogenetic mapping of facial nerve responses (blue laser, 10
641 ms, 2.0 mW) in a Thy1-ChR2 mouse. Averaged responses (> 5 trials) were normalized to the
642 range of 0 and 1 (right).

643
644 **Figure 6—figure supplement 6.** Optogenetic mapping of facial nerve responses (blue laser, 10
645 ms, 2.0 mW) in a Thy1-ChR2 mouse. Averaged responses (> 5 trials) were normalized to the
646 range of 0 and 1 (right).

647
648 **Figure 6—figure supplement 7.** Optogenetic mapping of facial nerve responses (blue laser, 10
649 ms, 2.0 mW) in a Thy1-ChR2 mouse. Averaged responses (> 5 trials) were normalized to the
650 range of 0 and 1 (right).

651

652 **References**

- 653 Alivisatos, A.P. *et al.* (2012) ‘The brain activity map project and the challenge of functional
654 connectomics’, *Neuron*, 74(6), pp. 970–974.
- 655 Amunts, K. *et al.* (2022) ‘Linking Brain Structure, Activity, and Cognitive Function through
656 Computation’, *eNeuro*, 9(2). Available at: <https://doi.org/10.1523/ENEURO.0316-21.2022>.
- 657 Andersen, R.A. (1989) ‘Visual and eye movement functions of the posterior parietal cortex’,
658 *Annual review of neuroscience*, 12, pp. 377–403.
- 659 Archambault, P.S., Caminiti, R. and Battaglia-Mayer, A. (2009) ‘Cortical mechanisms for online
660 control of hand movement trajectory: the role of the posterior parietal cortex’, *Cerebral cortex* ,
661 19(12), pp. 2848–2864.
- 662 Arenkiel, B.R. *et al.* (2007) ‘In Vivo Light-Induced Activation of Neural Circuitry in Transgenic
663 Mice Expressing Channelrhodopsin-2’, *Neuron*, pp. 205–218. Available at:
664 <https://doi.org/10.1016/j.neuron.2007.03.005>.
- 665 Aru, J., Suzuki, M. and Larkum, M.E. (2020) ‘Cellular Mechanisms of Conscious Processing’,
666 *Trends in cognitive sciences*, 24(10), pp. 814–825.
- 667 Auffret, M. *et al.* (2018) ‘Optogenetic stimulation of cortex to map evoked whisker movements
668 in awake head-restrained mice’, *Neuroscience*, 368, pp. 199–213.
- 669 Ayling, O.G.S. *et al.* (2009) ‘Automated light-based mapping of motor cortex by photoactivation
670 of channelrhodopsin-2 transgenic mice’, *Nature methods*, 6(3), pp. 219–224.
- 671 Barson, D. *et al.* (no date) ‘Simultaneous mesoscopic and two-photon imaging of neuronal
672 activity in cortical circuits’. Available at: <https://doi.org/10.1101/468348>.
- 673 Battaglia, F.P. *et al.* (2009) ‘The Lantern: an ultra-light micro-drive for multi-tetrode recordings
674 in mice and other small animals’, *Journal of neuroscience methods*, 178(2), pp. 291–300.
- 675 Billard, M.W. *et al.* (2018) ‘The systemDrive: a Multisite, Multiregion Microdrive with
676 Independent Drive Axis Angling for Chronic Multimodal Systems Neuroscience Recordings in
677 Freely Behaving Animals’, *eNeuro*, 5(6). Available at: <https://doi.org/10.1523/ENEURO.0261-18.2018>.
- 679 Blondel, V.D. *et al.* (2008) ‘Fast unfolding of communities in large networks’, *Journal of*
680 *statistical mechanics* , 2008(10), p. P10008.
- 681 Bragin, A. *et al.* (2000) ‘Multiple site silicon-based probes for chronic recordings in freely
682 moving rats: implantation, recording and histological verification’, *Journal of neuroscience*
683 *methods*, 98(1), pp. 77–82.
- 684 Brecht, M. *et al.* (2004) ‘Whisker movements evoked by stimulation of single pyramidal cells in
685 rat motor cortex’, *Nature*, 427(6976), pp. 704–710.

- 686 Buzsaki, G. (2006) *Rhythms of the Brain*. Oxford University Press.
- 687 Cembrowski, M.S. *et al.* (2016) ‘Hipposeq: a comprehensive RNA-seq database of gene
688 expression in hippocampal principal neurons’, *eLife*, 5, p. e14997.
- 689 Chapman, H. *et al.* (2002) ‘Posterior parietal cortex control of reach-to-grasp movements in
690 humans’, *The European journal of neuroscience*, 15(12), pp. 2037–2042.
- 691 Chen, J.L. *et al.* (2013) ‘Behaviour-dependent recruitment of long-range projection neurons in
692 somatosensory cortex’, *Nature*, 499(7458), pp. 336–340.
- 693 Chen, T.-W. *et al.* (2013) ‘Ultrasensitive fluorescent proteins for imaging neuronal activity’,
694 *Nature*, 499(7458), pp. 295–300.
- 695 Clancy, K.B., Orsolic, I. and Mrsic-Flogel, T.D. (2019) ‘Locomotion-dependent remapping of
696 distributed cortical networks’, *Nature neuroscience*, 22(5), pp. 778–786.
- 697 Cohen, Y.E. and Andersen, R.A. (2002) ‘A common reference frame for movement plans in the
698 posterior parietal cortex’, *Nature reviews. Neuroscience*, 3(7), pp. 553–562.
- 699 Delcasso, S. *et al.* (2018) ‘HOPE: Hybrid-Drive Combining Optogenetics, Pharmacology and
700 Electrophysiology’, *Frontiers in neural circuits*, 12, p. 41.
- 701 Egan, G.F. *et al.* (2015) ‘Average wild-type C57BL/6J mouse 3D MRI brain image’. Available
702 at: <https://espace.library.uq.edu.au/view/UQ:370299>.
- 703 Grinevich, V., Brecht, M. and Osten, P. (2005) ‘Monosynaptic pathway from rat vibrissa motor
704 cortex to facial motor neurons revealed by lentivirus-based axonal tracing’, *The Journal of
705 neuroscience: the official journal of the Society for Neuroscience*, 25(36), pp. 8250–8258.
- 706 Gutierrez-Barragan, D. *et al.* (2022) ‘Unique spatiotemporal fMRI dynamics in the awake mouse
707 brain’, *Current biology: CB*, 32(3), pp. 631–644.e6.
- 708 Hong, G. and Lieber, C.M. (2019) ‘Novel electrode technologies for neural recordings’, *Nature
709 Reviews Neuroscience*, pp. 330–345. Available at: <https://doi.org/10.1038/s41583-019-0140-6>.
- 710 Houweling, A.R. and Brecht, M. (2008) ‘Behavioural report of single neuron stimulation in
711 somatosensory cortex’, *Nature*, 451(7174), pp. 65–68.
- 712 Huber, D. *et al.* (2012) ‘Multiple dynamic representations in the motor cortex during
713 sensorimotor learning’, *Nature*, 484(7395), pp. 473–478.
- 714 Jiang, X. *et al.* (2015) ‘Principles of connectivity among morphologically defined cell types in
715 adult neocortex’, *Science*, 350(6264), p. aac9462.
- 716 Juavinett, A.L., Bekheet, G. and Churchland, A.K. (2019) ‘Chronically implanted Neuropixels
717 probes enable high-yield recordings in freely moving mice’, *eLife*, 8. Available at:
718 <https://doi.org/10.7554/eLife.47188>.

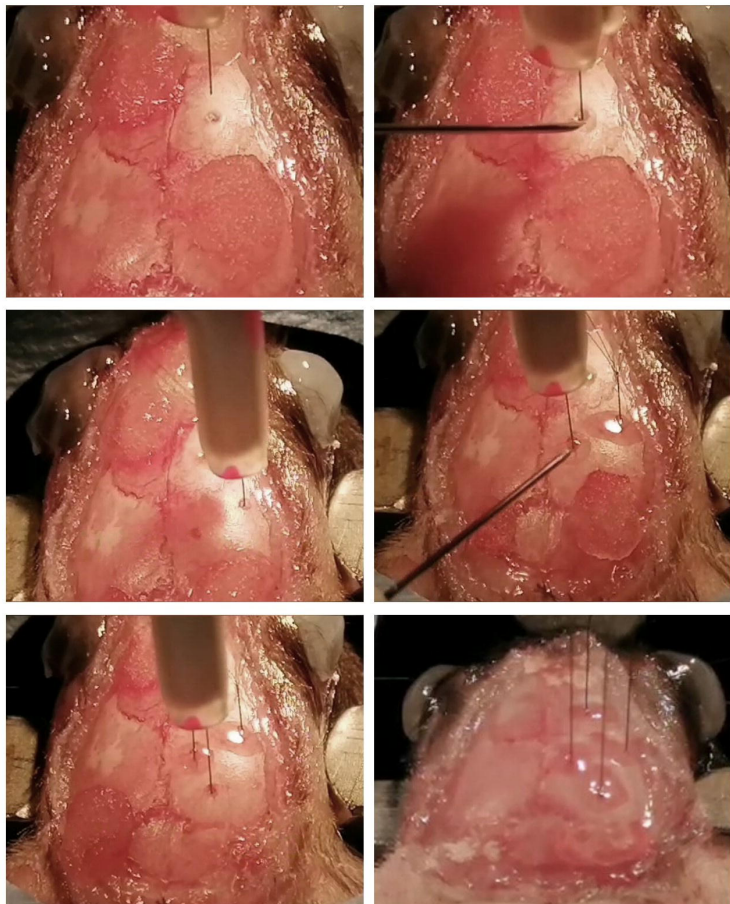
- 719 Karimi Abadchi, J. *et al.* (2020) ‘Spatiotemporal patterns of neocortical activity around
720 hippocampal sharp-wave ripples’, *eLife*, 9. Available at: <https://doi.org/10.7554/eLife.51972>.
- 721 Kim, H., Br nner, H.S. and Carl n, M. (2020) ‘The DMCdrive: practical 3D-printable micro-
722 drive system for reliable chronic multi-tetrode recording and optogenetic application in freely
723 behaving rodents’, *Scientific reports*, 10(1), p. 11838.
- 724 Koch, C. *et al.* (2016) ‘Neural correlates of consciousness: progress and problems’, *Nature*
725 *reviews. Neuroscience*, 17(5), pp. 307–321.
- 726 Konen, C.S. and Kastner, S. (2008) ‘Representation of eye movements and stimulus motion in
727 topographically organized areas of human posterior parietal cortex’, *The Journal of*
728 *neuroscience: the official journal of the Society for Neuroscience*, 28(33), pp. 8361–8375.
- 729 Lee, J.J. *et al.* (2022) ‘Task specificity in mouse parietal cortex’, *Neuron*, 110(18), pp. 2961–
730 2969.e5.
- 731 Levine, J.H. *et al.* (2015) ‘Data-Driven Phenotypic Dissection of AML Reveals Progenitor-like
732 Cells that Correlate with Prognosis’, *Cell*, 162(1), pp. 184–197.
- 733 Liu, X. *et al.* (2021) ‘Multimodal neural recordings with Neuro-FITM uncover diverse patterns
734 of cortical–hippocampal interactions’, *Nature neuroscience*, 24(6), pp. 886–896.
- 735 Liu, X., Leopold, D.A. and Yang, Y. (2021) ‘Single-neuron firing cascades underlie global
736 spontaneous brain events’, *Proceedings of the National Academy of Sciences of the United States*
737 *of America*, 118(47). Available at: <https://doi.org/10.1073/pnas.2105395118>.
- 738 Lyamzin, D. and Benucci, A. (2019) ‘The mouse posterior parietal cortex: Anatomy and
739 functions’, *Neuroscience research*, 140, pp. 14–22.
- 740 Lynch, J.C. (1980) ‘The functional organization of posterior parietal association cortex’, *The*
741 *Behavioral and brain sciences*, 3(4), pp. 485–499.
- 742 Margolis, D.J. *et al.* (2012) ‘Reorganization of cortical population activity imaged throughout
743 long-term sensory deprivation’, *Nature neuroscience*, 15(11), pp. 1539–1546.
- 744 Matyas, F. *et al.* (2010) ‘Motor control by sensory cortex’, *Science*, 330(6008), pp. 1240–1243.
- 745 Mercer Lindsay, N. *et al.* (2019) ‘Orofacial Movements Involve Parallel Corticobulbar
746 Projections from Motor Cortex to Trigeminal Premotor Nuclei’, *Neuron*, 104(4), pp. 765–780.e3.
- 747 Mohajerani, M.H. *et al.* (2013) ‘Spontaneous cortical activity alternates between motifs defined
748 by regional axonal projections’, *Nature neuroscience*, 16(10), pp. 1426–1435.
- 749 Nguyen, D.P. *et al.* (2009) ‘Micro-drive array for chronic in vivo recording: tetrode assembly’,
750 *Journal of Visualized Experiments* [Preprint]. Available at: <https://doi.org/10.3791/1098>.
- 751 Oh, S.W. *et al.* (2014) ‘A mesoscale connectome of the mouse brain’, *Nature*, 508(7495), pp.

- 752 207–214.
- 753 Packer, A.M. *et al.* (2015) ‘Simultaneous all-optical manipulation and recording of neural circuit
754 activity with cellular resolution in vivo’, *Nature methods*, 12(2), pp. 140–146.
- 755 Pessoa, L. (2014) ‘Understanding brain networks and brain organization’, *Physics of life reviews*,
756 11(3), pp. 400–435.
- 757 Peters, A.J. *et al.* (2021) ‘Striatal activity topographically reflects cortical activity’, *Nature*,
758 591(7850), pp. 420–425.
- 759 Petersen, C.C.H. (2014) ‘Cortical control of whisker movement’, *Annual review of neuroscience*,
760 37, pp. 183–203.
- 761 Phillips, D.P. and Irvine, D.R. (1979) ‘Acoustic input to single neurons in pulvinar-posterior
762 complex of cat thalamus’, *Journal of neurophysiology*, 42(1 Pt 1), pp. 123–136.
- 763 Pouget, P. (2015) ‘The cortex is in overall control of “voluntary” eye movement’, *Eye*, 29(2),
764 pp. 241–245.
- 765 Rancz, E.A. *et al.* (2007) ‘High-fidelity transmission of sensory information by single cerebellar
766 mossy fibre boutons’, *Nature*, 450(7173), pp. 1245–1248.
- 767 Rathelot, J.-A., Dum, R.P. and Strick, P.L. (2017) ‘Posterior parietal cortex contains a command
768 apparatus for hand movements’, *Proceedings of the National Academy of Sciences of the United
769 States of America*, 114(16), pp. 4255–4260.
- 770 Roth, R.H. and Ding, J.B. (2020) ‘From neurons to cognition: Technologies for precise recording
771 of neural activity underlying behavior’, *BME Frontiers*, 2020, pp. 1–20.
- 772 Rousseeuw, P.J. (1987) ‘Silhouettes: A graphical aid to the interpretation and validation of
773 cluster analysis’, *Journal of computational and applied mathematics*, 20, pp. 53–65.
- 774 Sakata, H. *et al.* (1997) ‘The TINS Lecture. The parietal association cortex in depth perception
775 and visual control of hand action’, *Trends in neurosciences*, 20(8), pp. 350–357.
- 776 Silasi, G. *et al.* (2016) ‘Intact skull chronic windows for mesoscopic wide-field imaging in
777 awake mice’, *Journal of neuroscience methods*, 267, pp. 141–149.
- 778 Sreenivasan, V. *et al.* (2016) ‘Movement Initiation Signals in Mouse Whisker Motor Cortex’,
779 *Neuron*, 92(6), pp. 1368–1382.
- 780 Steinmetz, N.A. *et al.* (2021) ‘Neuropixels 2.0: A miniaturized high-density probe for stable,
781 long-term brain recordings’, *Science*, 372(6539). Available at:
782 <https://doi.org/10.1126/science.abf4588>.
- 783 Swindale, N.V. *et al.* (2021) ‘Voltage distributions in extracellular brain recordings’, *Journal of
784 neurophysiology*, 125(4), pp. 1408–1424.

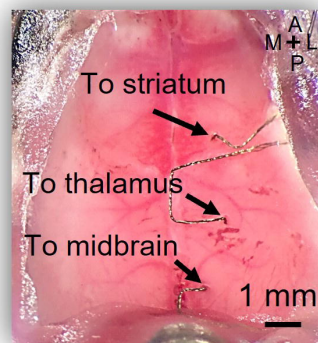
- 785 Swindale, N.V. and Spacek, M.A. (2014) ‘Spike sorting for polytrodes: a divide and conquer
786 approach’, *Frontiers in systems neuroscience*, 8, p. 6.
- 787 Tolias, A.S. *et al.* (2007) ‘Recording chronically from the same neurons in awake, behaving
788 primates’, *Journal of neurophysiology*, 98(6), pp. 3780–3790.
- 789 Vandecasteele, M. *et al.* (2012) ‘Large-scale Recording of Neurons by Movable Silicon Probes
790 in Behaving Rodents’, *Journal of Visualized Experiments* [Preprint]. Available at:
791 <https://doi.org/10.3791/3568>.
- 792 Vanni, M.P. and Murphy, T.H. (2014) ‘Mesoscale transcranial spontaneous activity mapping in
793 GCaMP3 transgenic mice reveals extensive reciprocal connections between areas of
794 somatomotor cortex’, *The Journal of neuroscience: the official journal of the Society for
795 Neuroscience*, 34(48), pp. 15931–15946.
- 796 Voigts, J. *et al.* (2013) ‘The flexDrive: an ultra-light implant for optical control and highly
797 parallel chronic recording of neuronal ensembles in freely moving mice’, *Frontiers in systems
798 neuroscience*, 7, p. 8.
- 799 Voigts, J. *et al.* (2020) ‘An easy-to-assemble, robust, and lightweight drive implant for chronic
800 tetrode recordings in freely moving animals’, *Journal of neural engineering*, 17(2), p. 026044.
- 801 Voigts, J. and Harnett, M.T. (2020) ‘Somatic and Dendritic Encoding of Spatial Variables in
802 Retrosplenial Cortex Differs during 2D Navigation’, *Neuron*, 105(2), pp. 237–245.e4.
- 803 White, B.R. *et al.* (2011) ‘Imaging of functional connectivity in the mouse brain’, *PloS one*, 6(1),
804 p. e16322.
- 805 Xiao, D. *et al.* (2017) ‘Mapping cortical mesoscopic networks of single spiking cortical or sub-
806 cortical neurons’, *eLife*. Available at: <https://doi.org/10.7554/elife.19976>.
- 807 Xiao, D. *et al.* (2021) ‘MesoNet allows automated scaling and segmentation of mouse mesoscale
808 cortical maps using machine learning’, *Nature communications*, 12, p. 5992.
- 809 Zhao, S. *et al.* (2011) ‘Cell type-specific channelrhodopsin-2 transgenic mice for optogenetic
810 dissection of neural circuitry function’, *Nature methods*, 8(9), pp. 745–752.

A

Implantation of tetrodes to multiple targets

**B**

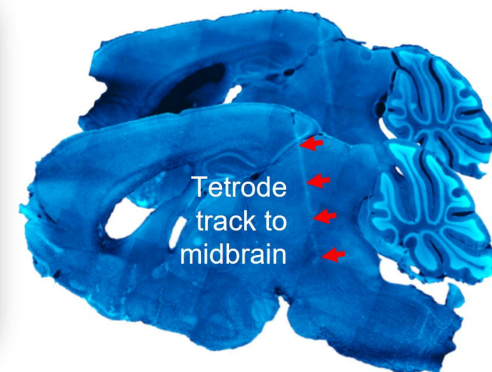
Transparent window

**C**

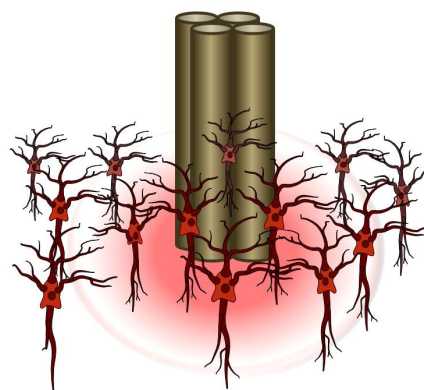
Group housing

**D**

Histology

**E**

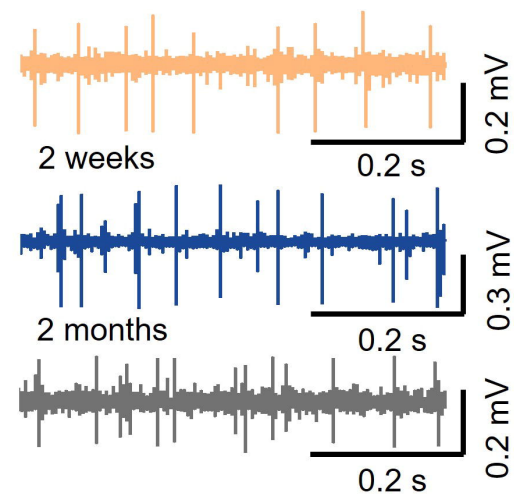
Tetrode

**F**

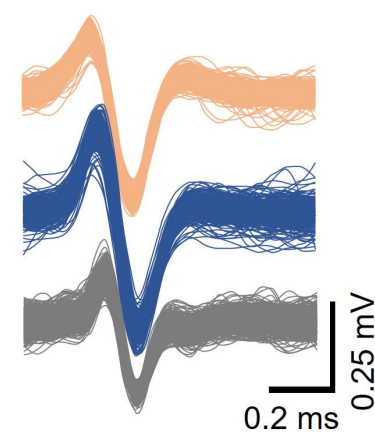
1 week

2 weeks

2 months

**G**

Single unit

**Figure 1.**

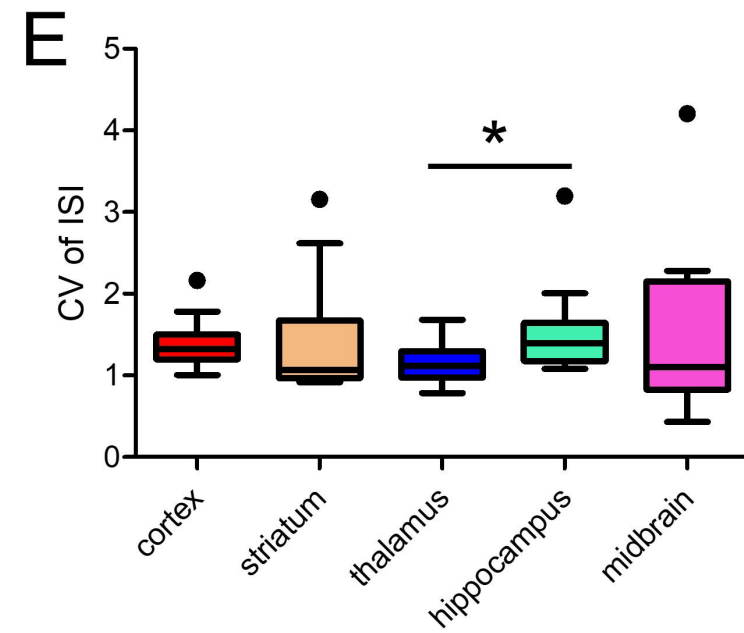
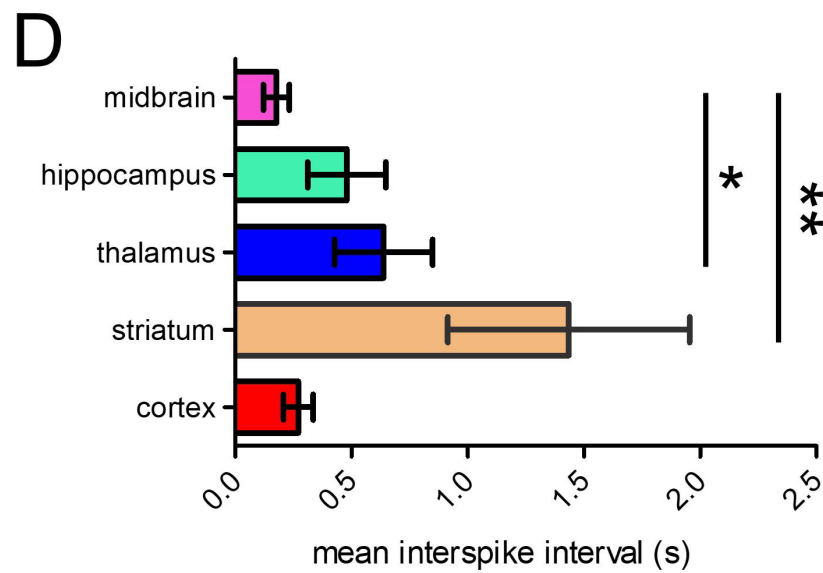
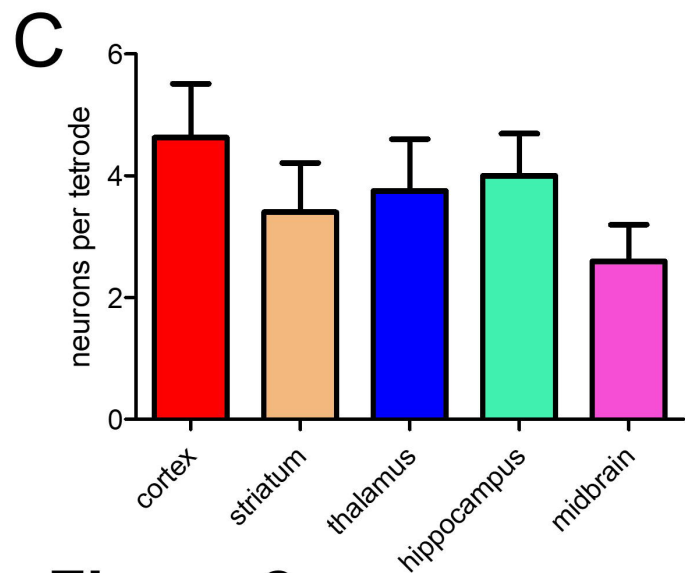
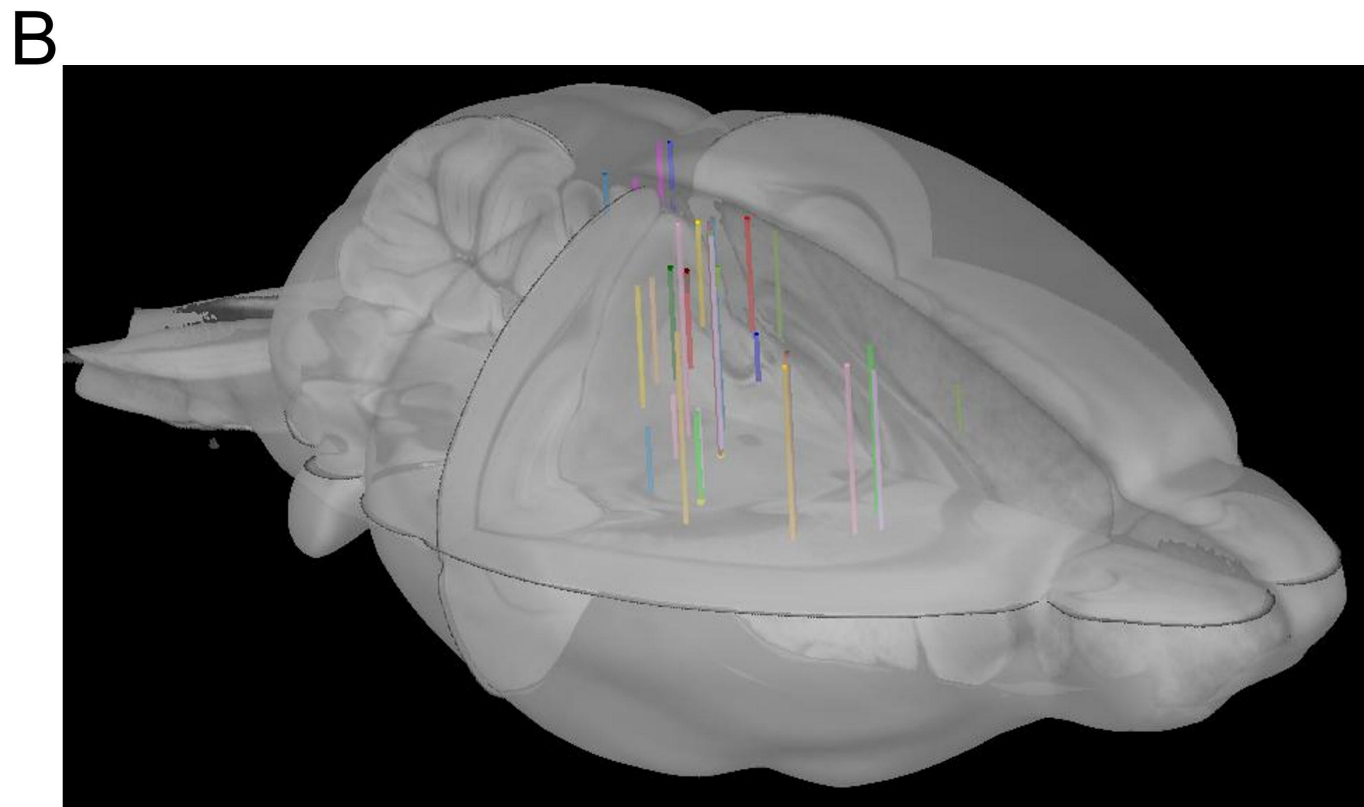
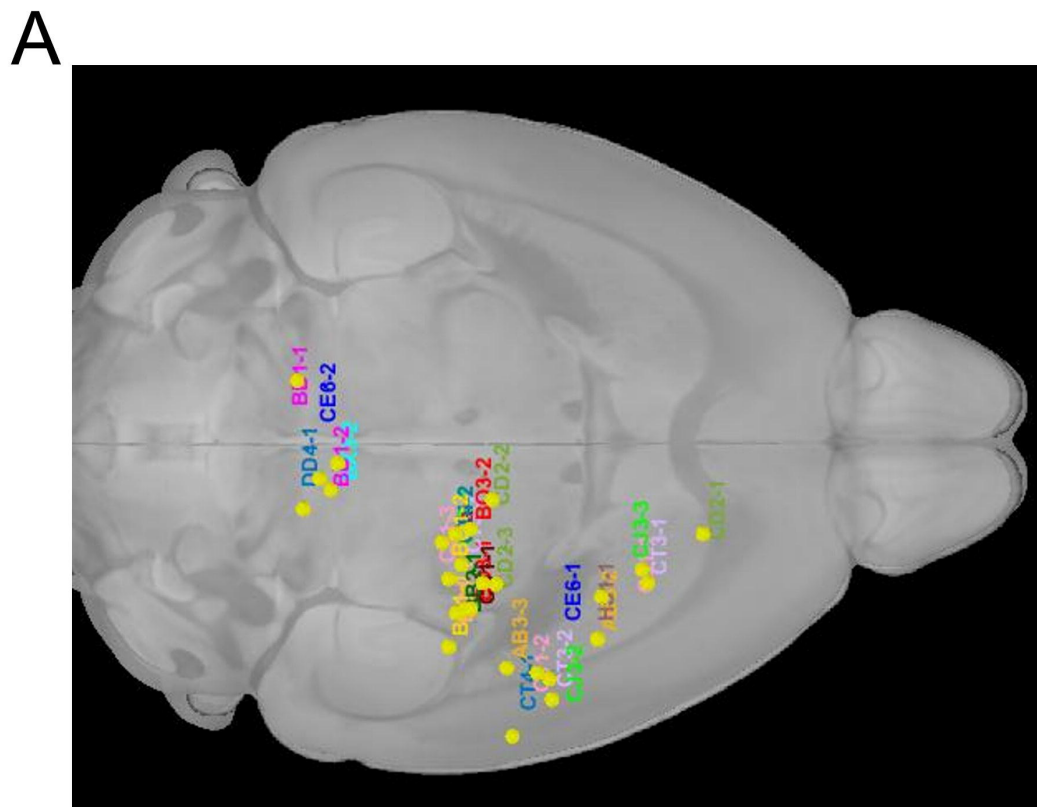


Figure 2.

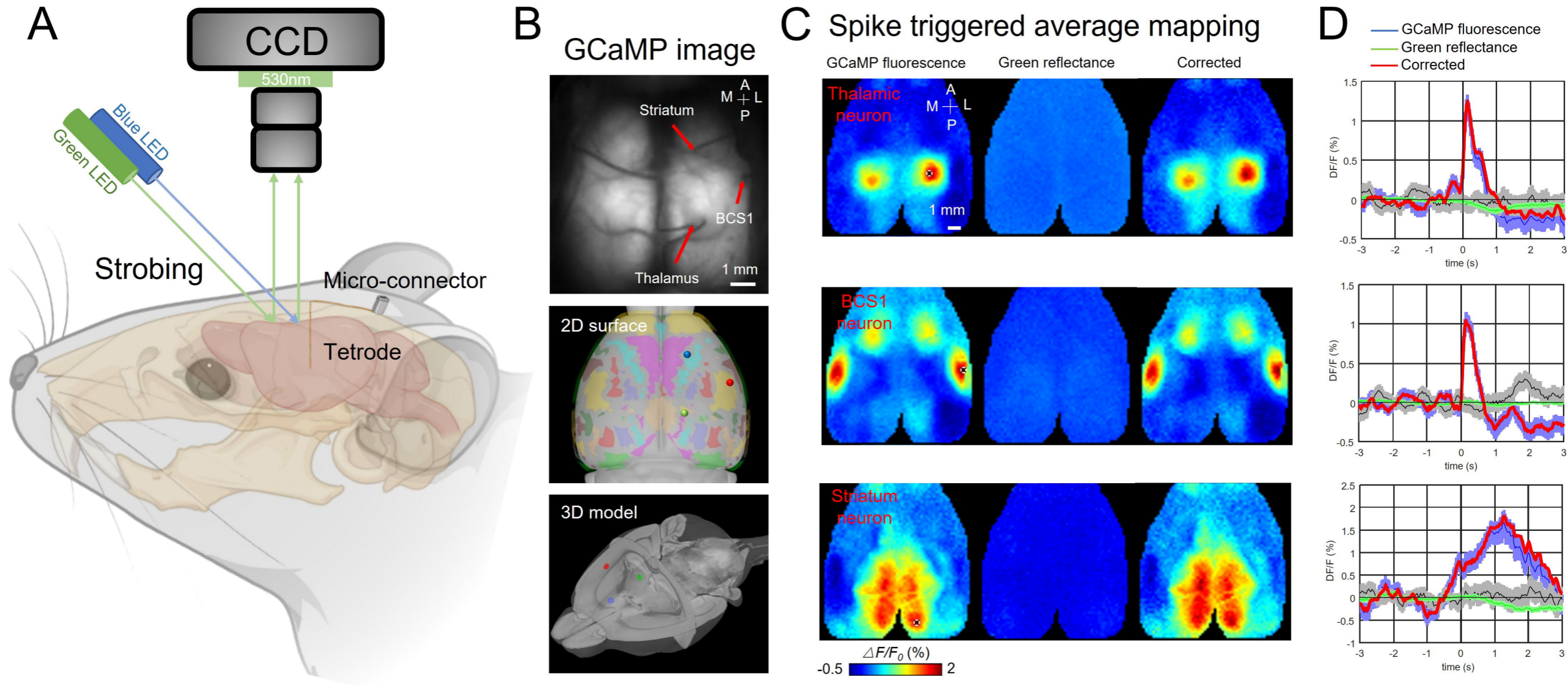


Figure 3.

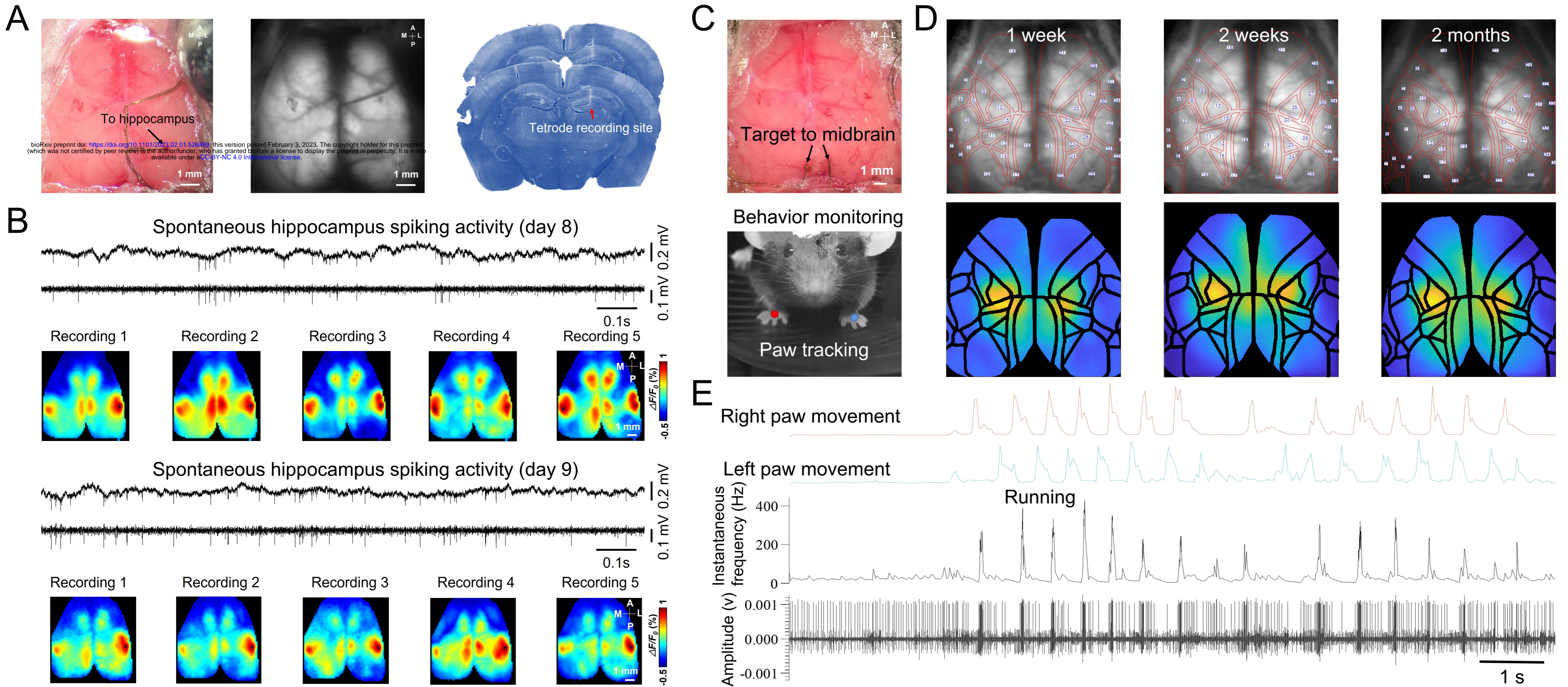


Figure 4.

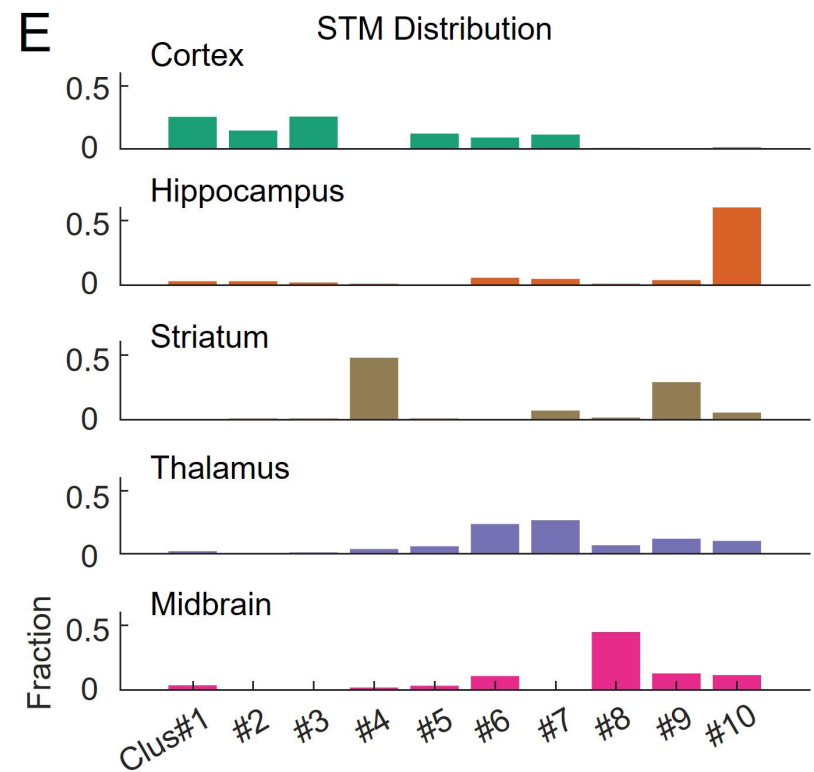
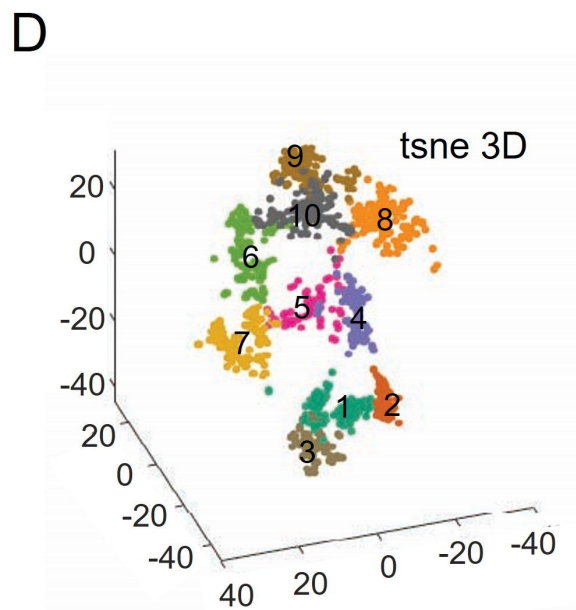
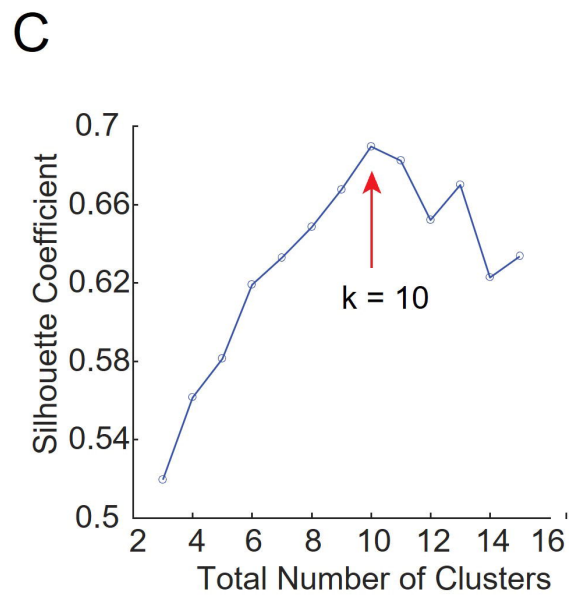
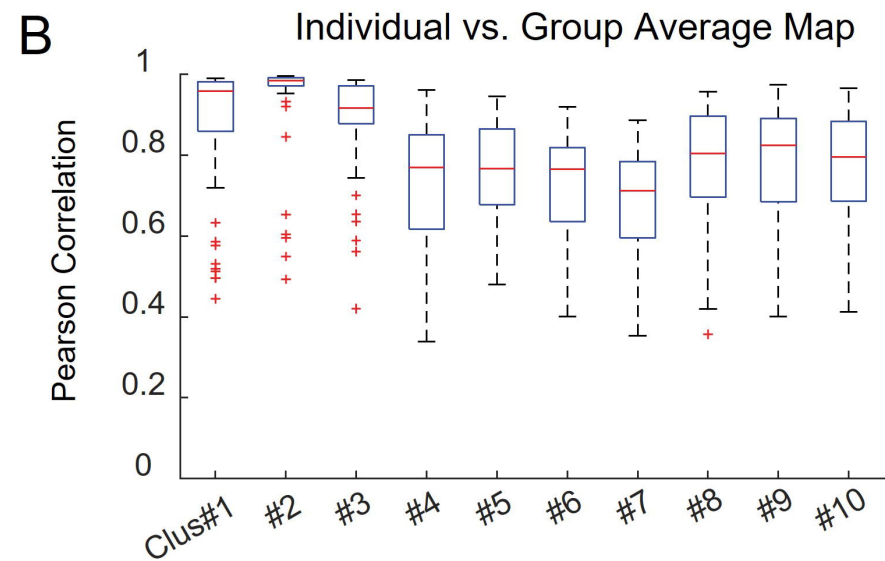
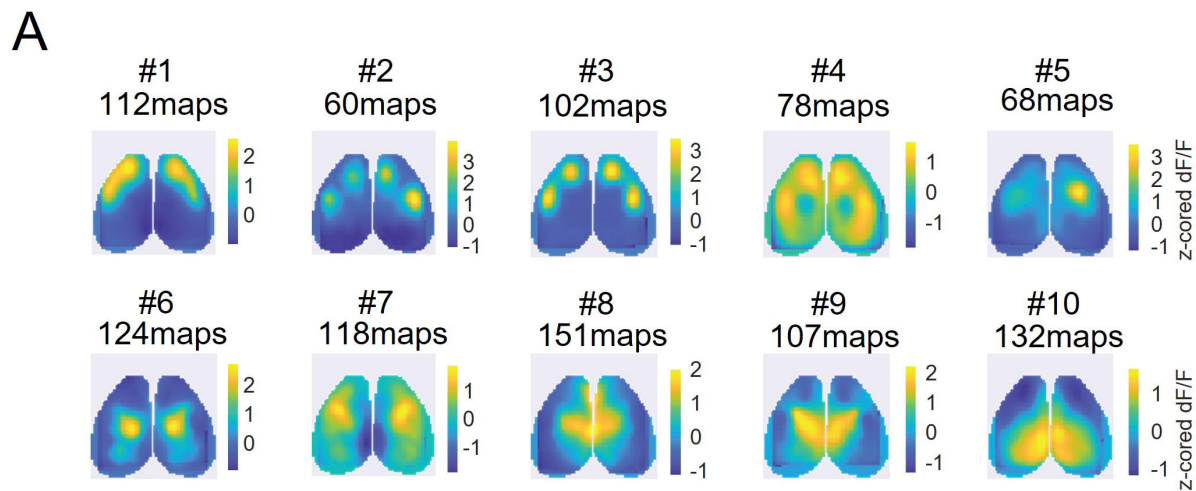


Figure 5.

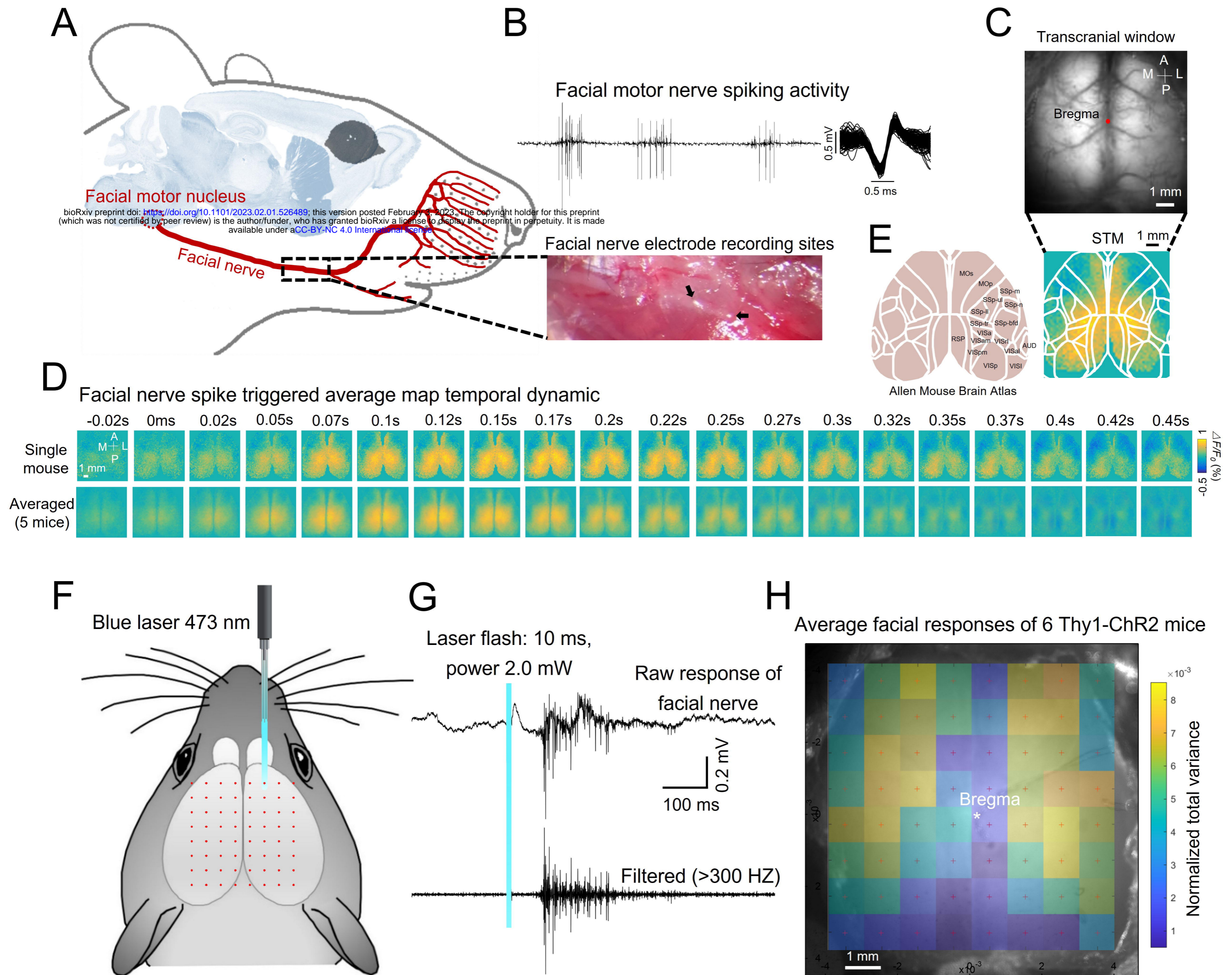
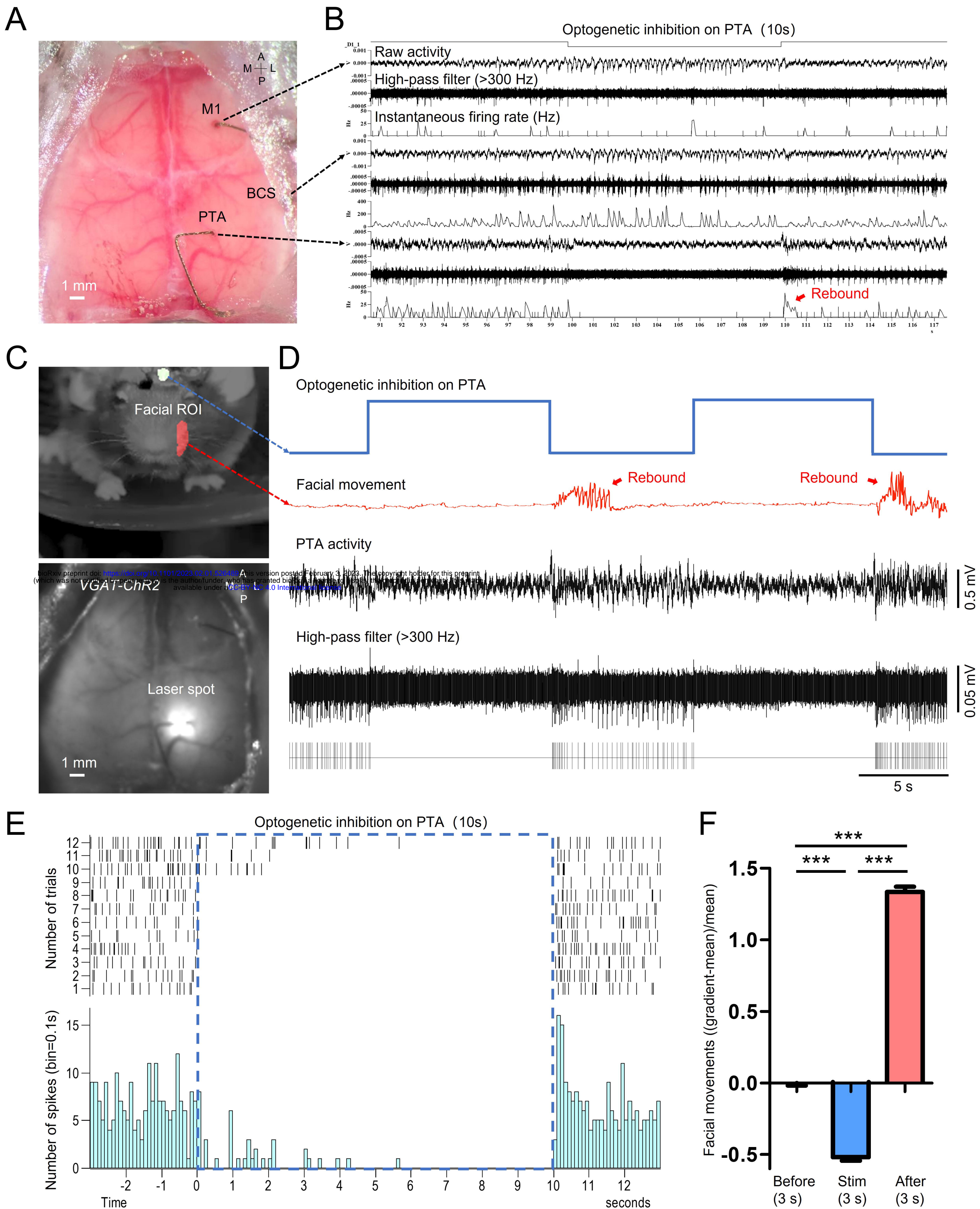
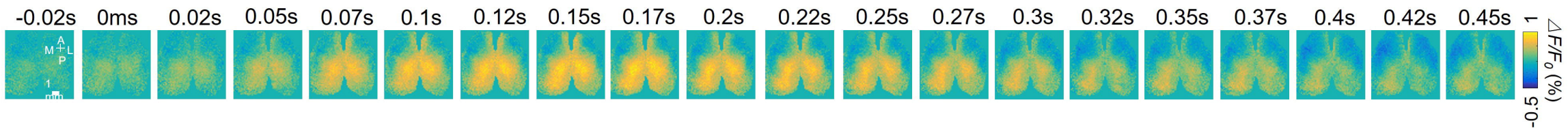


Figure 6.

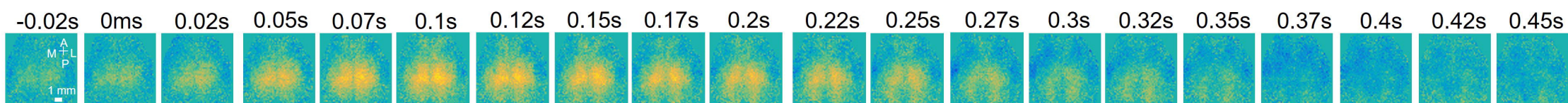


Facial nerve spike triggered average map temporal dynamic

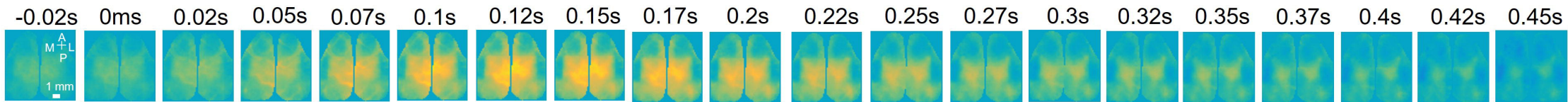
Mouse 1#



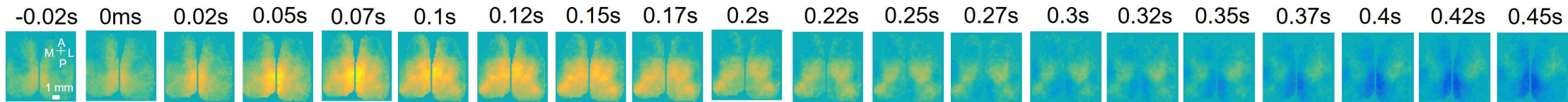
Mouse 2#



Mouse 3#



Mouse 4#



Mouse 5#

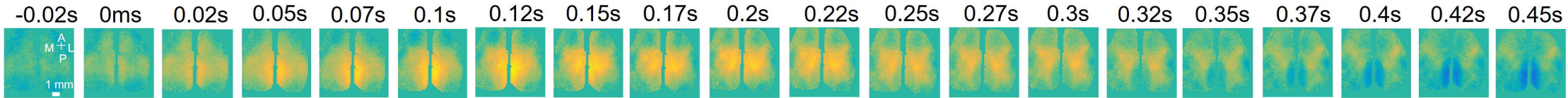


Figure 6—figure supplement 1.

MouseQE1

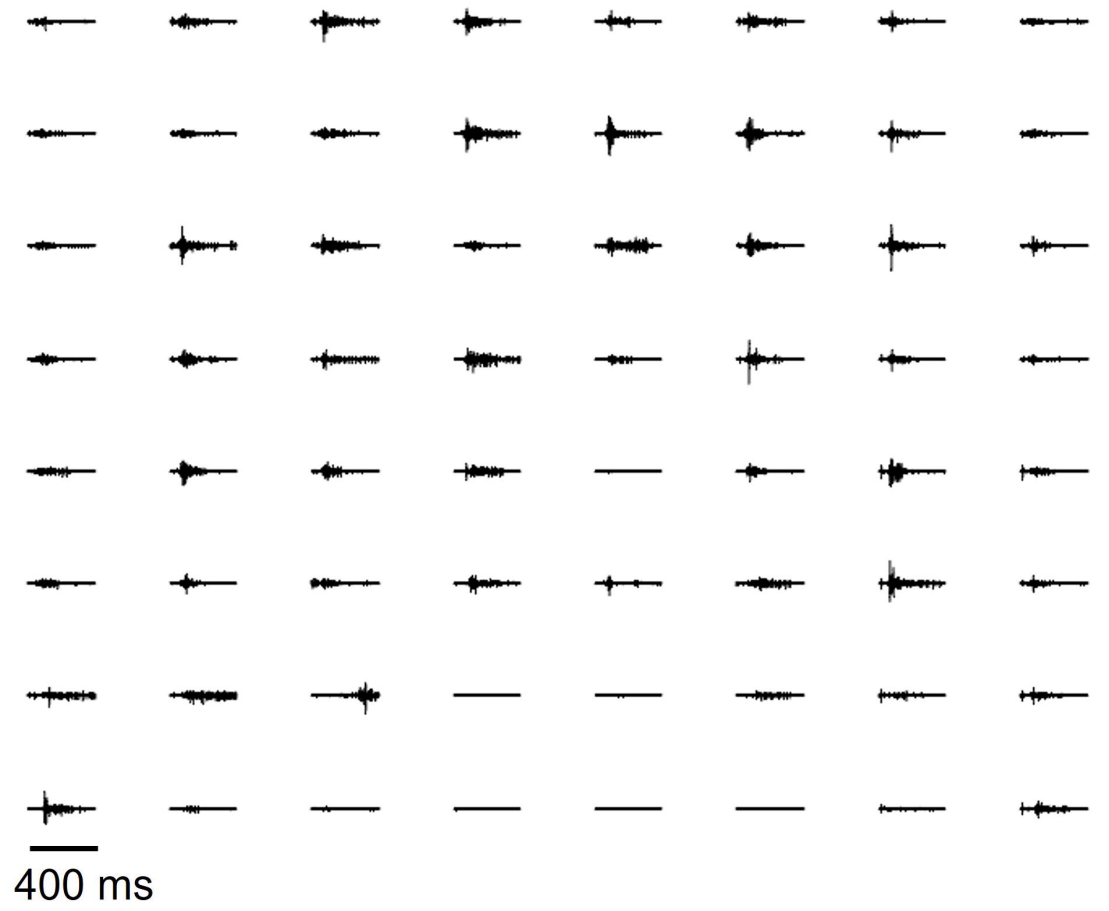
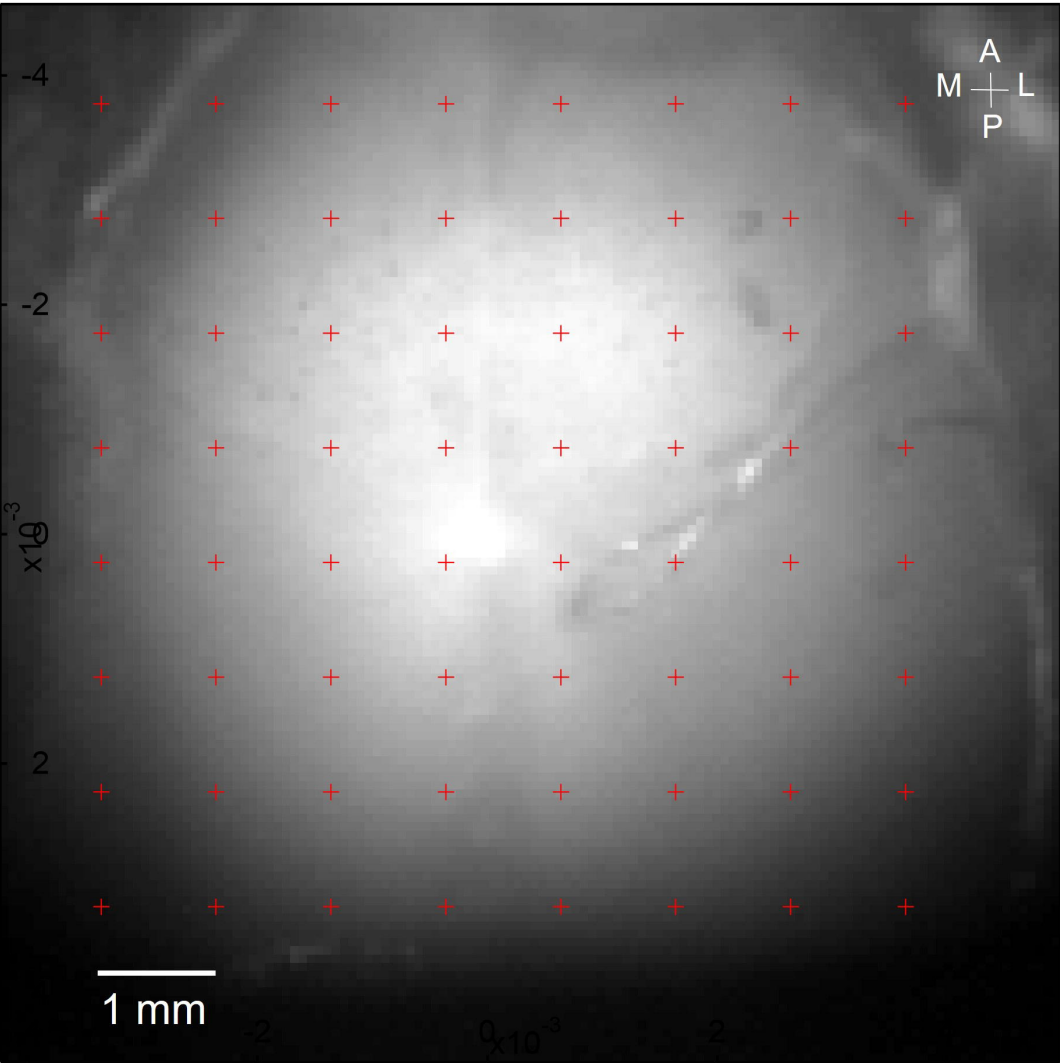


Figure 6—figure supplement 2.

MouseQE2

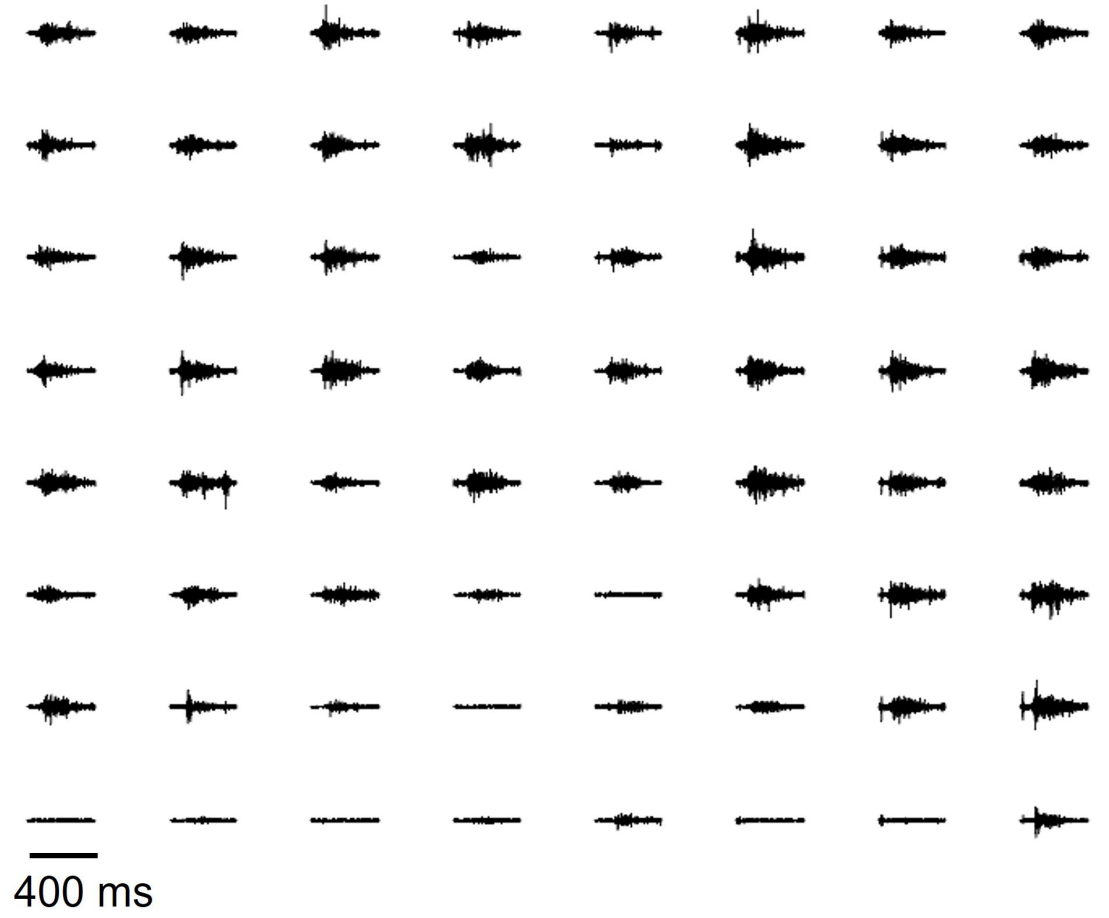
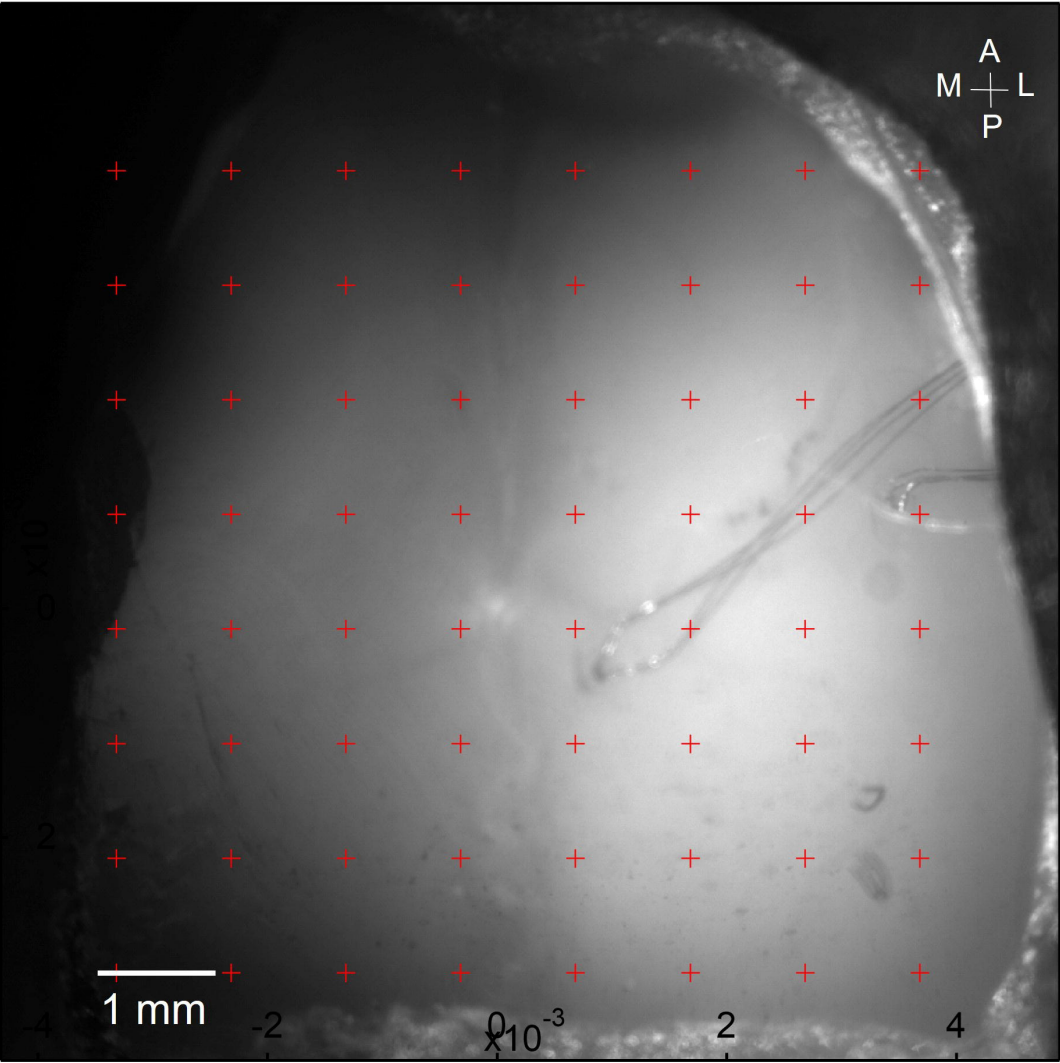


Figure 6—figure supplement 3.

MouseQN1

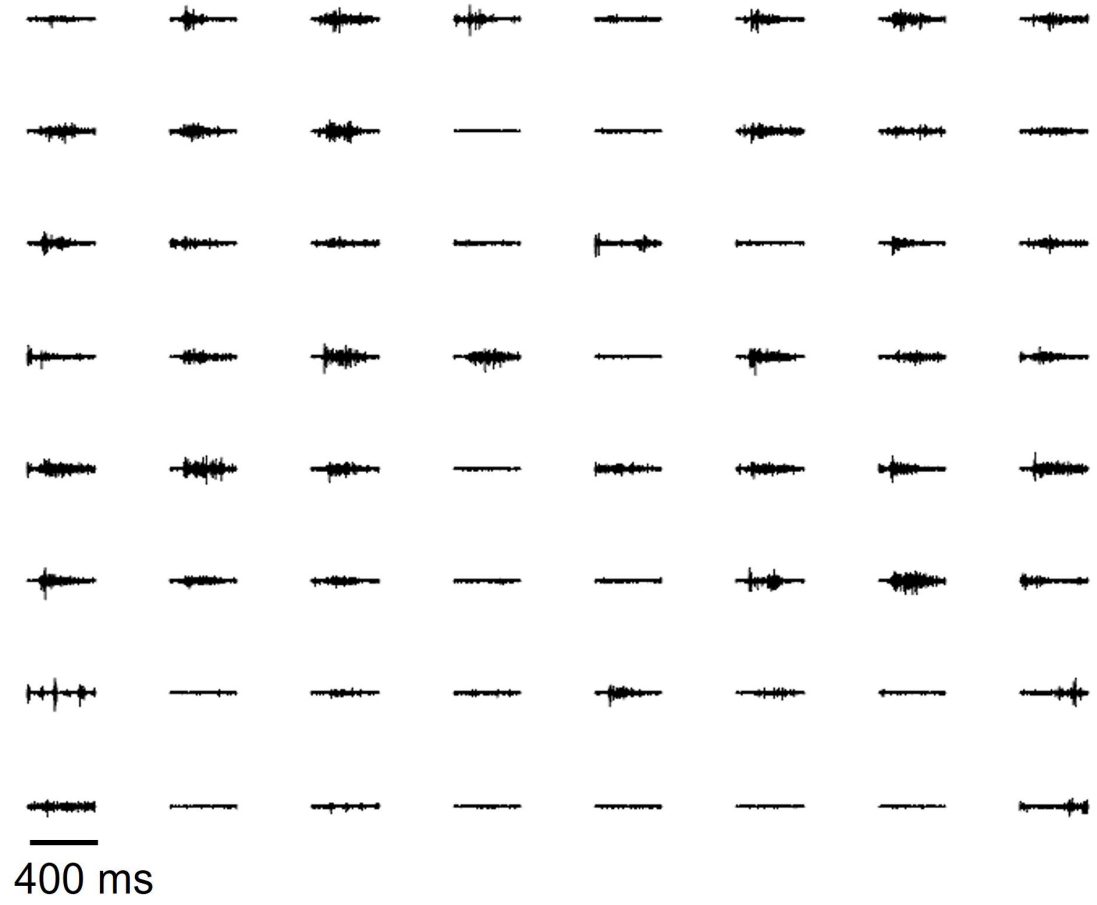
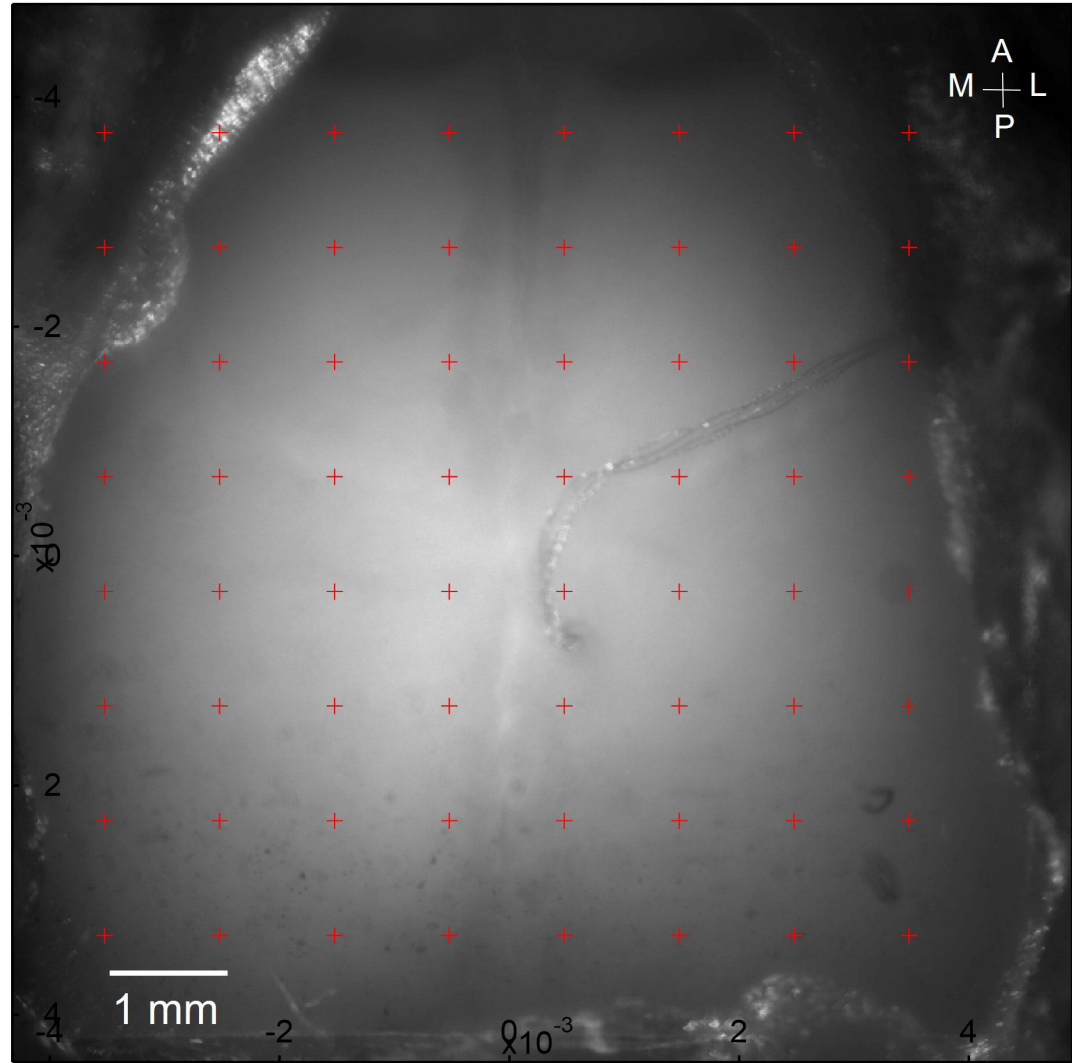


Figure 6—figure supplement 4.

MouseQN2

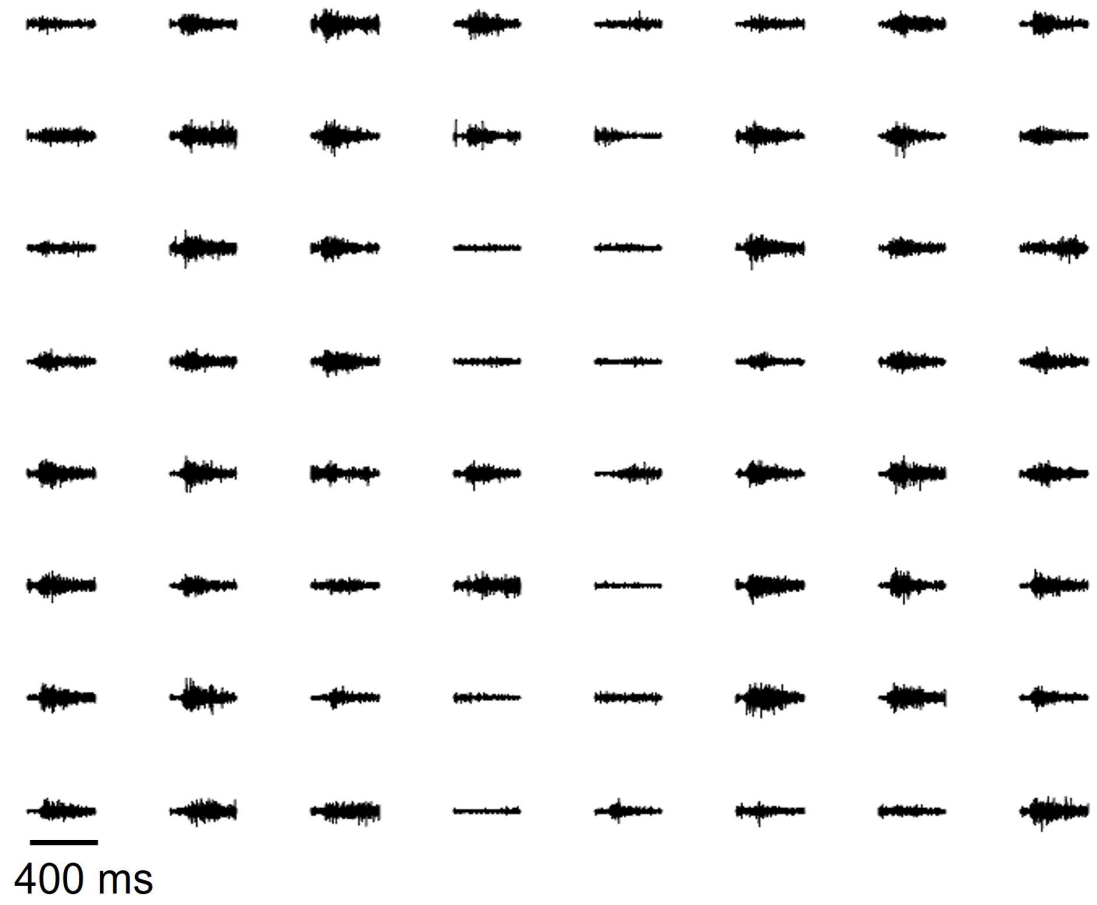
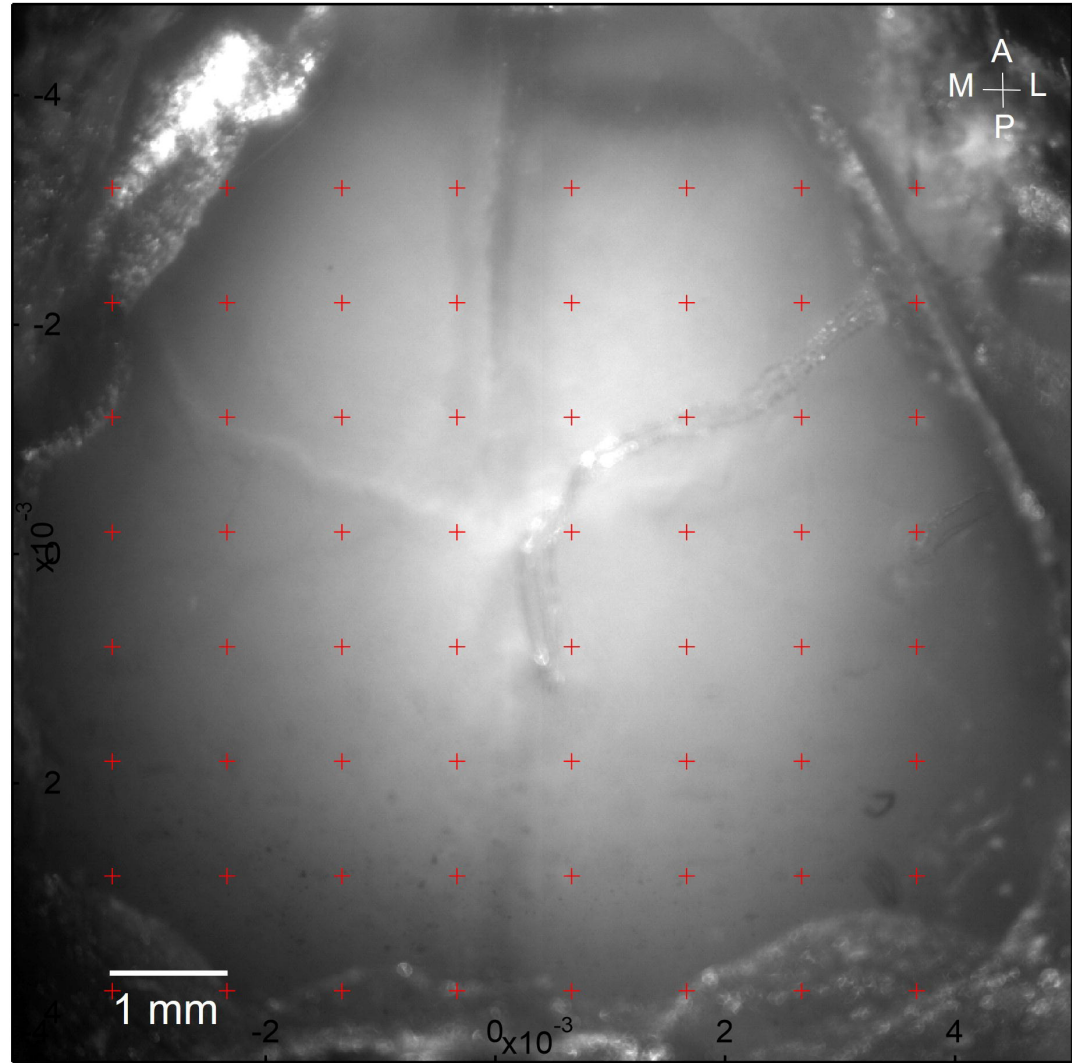


Figure 6—figure supplement 5.

MouseQN3

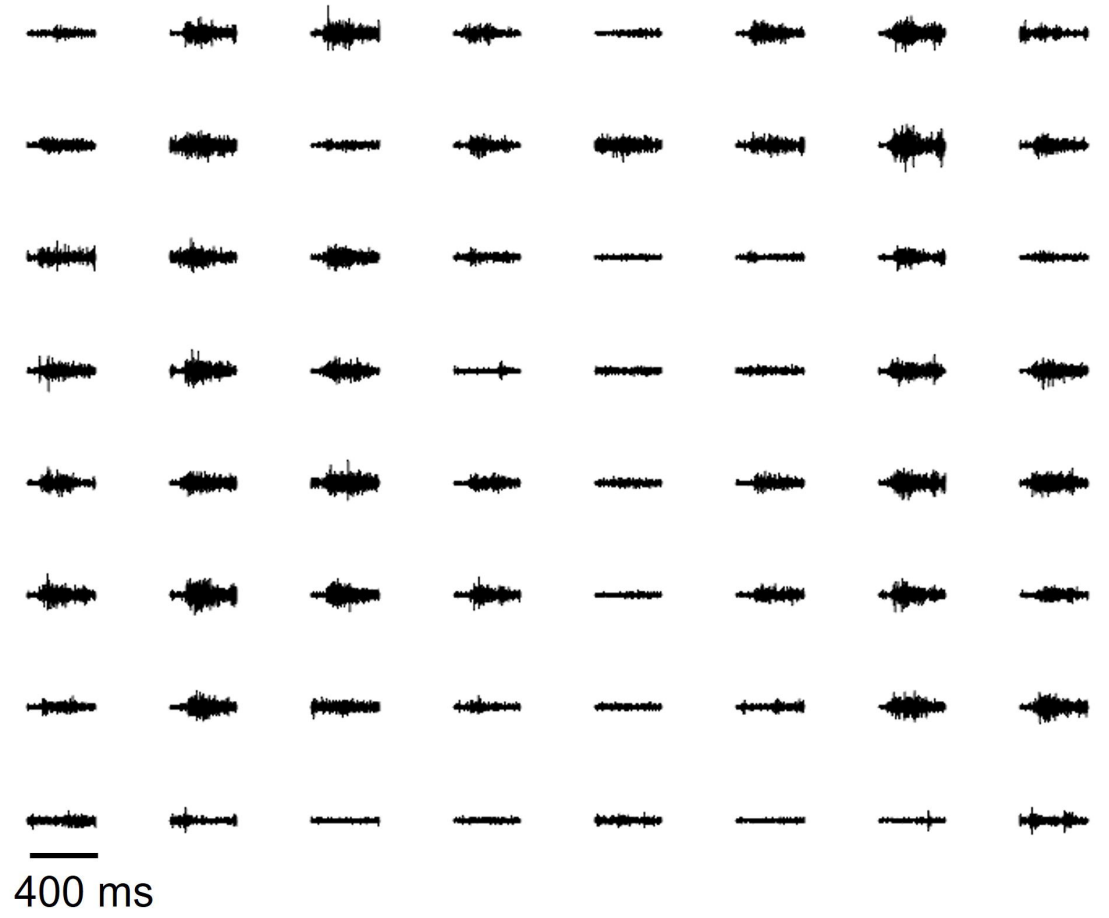
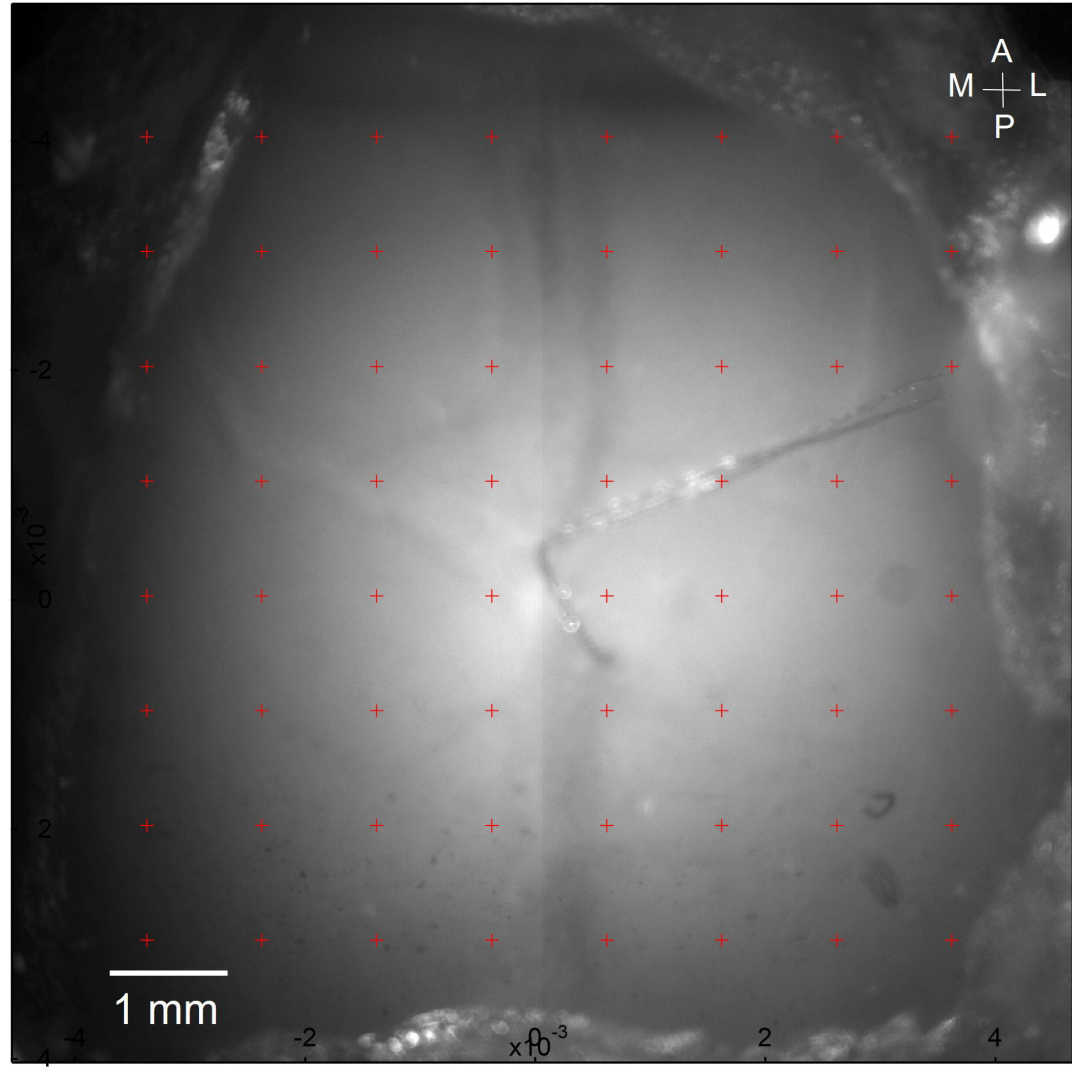


Figure 6—figure supplement 6.

MouseQN4

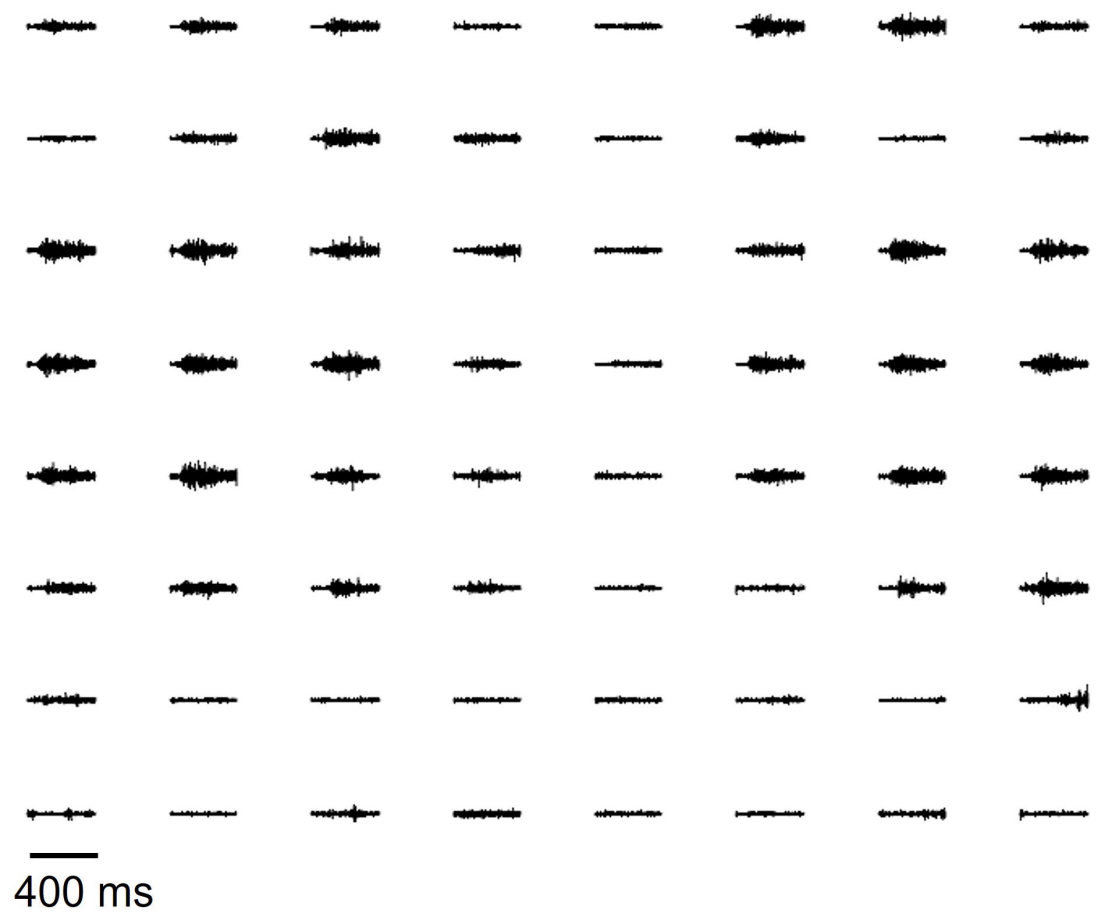
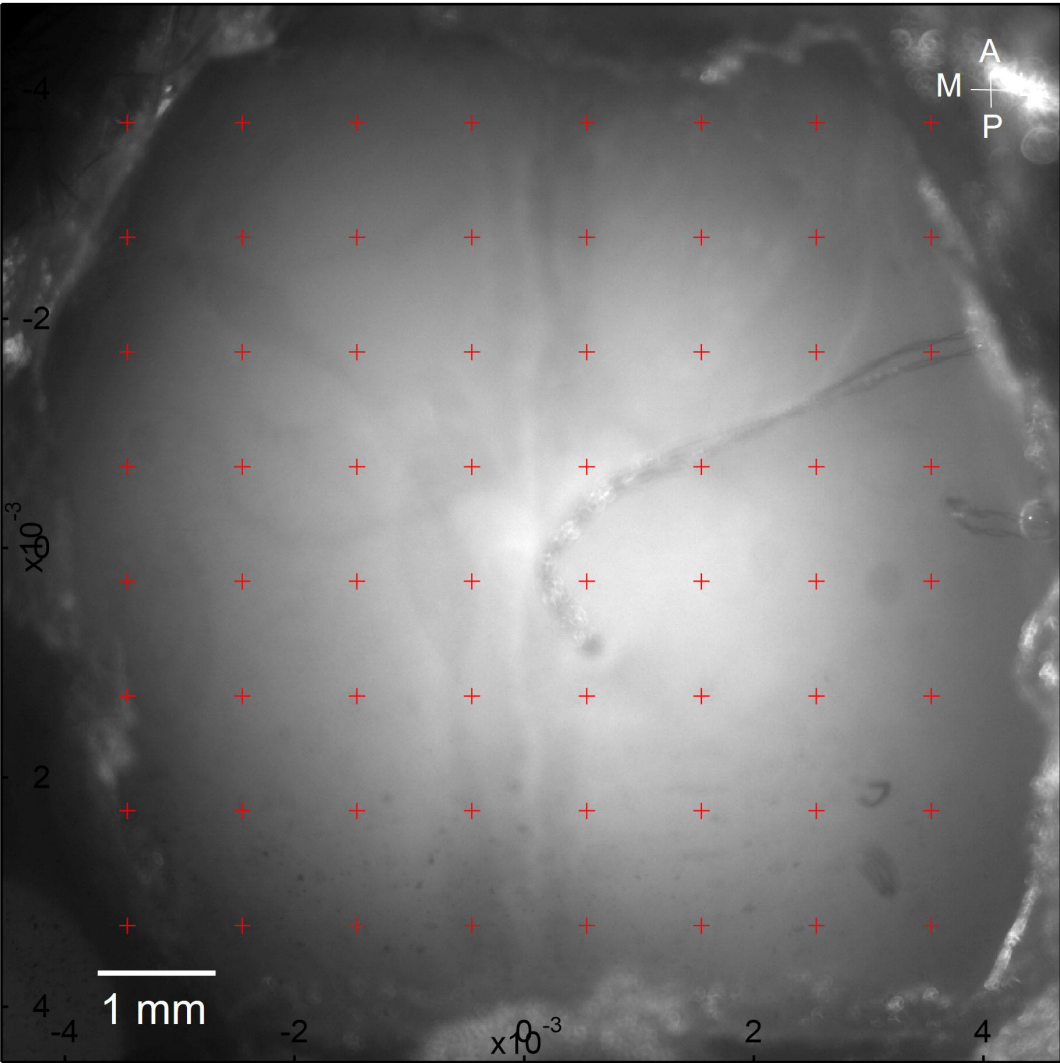


Figure 6—figure supplement 7.